Journal of Materials Chemistry A

ROYAL SOCIETY OF CHEMISTRY

PAPER

View Article Online
View Journal | View Issue

Cite this: J. Mater. Chem. A, 2025, 13, 41913

Synergistic engineering of anthracene- and thiazolo[5,4-*d*] thiazole-based donor–acceptor conjugated microporous polymers with heteroatom adoption for enhanced energy storage capacity

Abdul Basit,†[a] Mohamed Gamal Mohamed, †*[ab] Hira Karim [c] and Shiao-Wei Kuo *[ad]

Conventional supercapacitor electrodes are often hampered by low energy density, limited cycle life, and inadequate electrical conductivity. In contrast, conjugated microporous polymers (CMPs) represent an emerging class of electrode materials that simultaneously provide high surface areas, robust structural integrity, and enhanced electronic conductivity. Herein, we present the rational design and synthesis of two novel donor–acceptor (D–A) conjugated microporous polymers (CMPs) featuring a high density of heteroatoms [thiazolo[5,4-*d*]thiazole, TzTz] strategically embedded within the framework, namely ANPh-TzTz and ANTPh-TzTz, incorporating redox-active thiazolo[5,4-*d*]thiazole (TzTz) units as organic electrodes for supercapacitor applications *via* a condensation reaction between 2,3,6,7,9,10-hexa-(4-formylphenyl)anthracene (ANPh-6CHO) or 4,4′,4″,4‴-(anthracene-9,10-diylidenebis(methanediylylidene))tetrabenzaldehyde (ANTPh-4CHO) and dithiooxamide in *N*,*N*-dimethylformamide (DMF). Both materials have outstanding thermal stabilities and exhibit moderate Brunauer–Emmett–Teller (BET) surface areas. Electrochemical evaluation reveals that ANPh-TzTz CMP delivers an excellent specific capacitance of 541 F g^{-1} with a remarkable capacitance retention of 94% over extended cycling. Furthermore, symmetric coin cell devices constructed using ANPh-TzTz CMP as the active material exhibit outstanding electrochemical performance, achieving a high energy density of 16.1 Wh kg^{-1} at a power density of 705.9 W kg^{-1}, along with a device-level capacitance of 220 F g^{-1}. These results show how effective molecular engineering may be in creating next-generation CMP-based electrode materials and how promising they are for high-performance energy storage applications.

Received 6th July 2025
Accepted 7th November 2025

DOI: 10.1039/d5ta05442g

rsc.li/materials-a

Introduction

In the modern digital era, society is increasingly reliant on electronic devices, creating an ever-growing demand for a reliable energy supply and efficient storage systems. This energy demand is predominantly met by a mix of renewable sources—such as solar, wind, ocean, hydropower, and biomass—and non-renewable fossil fuels, including coal, natural gas, and petroleum.[1,2] Alarmingly, approximately 90% of carbon dioxide emissions in most countries stem from fossil fuel combustion, which collectively contributes to over 75% of global greenhouse gas emissions. Despite the promise of renewable energy, its inherent intermittency and dependence on environmental conditions limit its capacity to ensure the stable and continuous energy supply required for sustained economic development and digital infrastructure.[3–5] Striking an optimal balance between technological advancement, environmental stewardship, and uninterrupted energy delivery remains a critical challenge. Among energy storage technologies, supercapacitors (SCs) and rechargeable batteries have garnered significant attention. Batteries, although capable of high energy storage, suffer from limited cycling stability and environmental concerns associated with redox-active materials.[6,7] In contrast, supercapacitors, with their superior power density, rapid charge–discharge rates, and extended cycle life, represent a compelling and increasingly indispensable solution for addressing future energy storage demands.[8,9] Conventional batteries, while indispensable, are fundamentally constrained by their limited energy storage

[a]Department of Materials and Optoelectronic Science, Center for Functional Polymers and Supramolecular Materials, National Sun Yat-Sen University, Kaohsiung 804, Taiwan. E-mail: mgamal.eldin34@gmail.com; kuosw@faculty.nsysu.edu.tw

[b]Department of Chemistry, Faculty of Science, Assiut University, Assiut 71516, Egypt

[c]Department of Chemistry, School of Natural Sciences (SNS), National University of Sciences and Technology (NUST), H-12, Islamabad 44000, Pakistan

[d]Department of Medicinal and Applied Chemistry, Kaohsiung Medical University, Kaohsiung 807, Taiwan

† These authors contributed equally to this work.

capacity and relatively slow charge–discharge kinetics. In contrast, electrostatic capacitors—particularly supercapacitors (SCs)—offer exceptionally high power densities, unlocking significant potential for next-generation energy storage systems.[10,11] As global demand intensifies for compact, safe, and high-performance power solutions across commercial, military, and consumer sectors, the development of advanced energy storage technologies is becoming increasingly urgent and strategically important.[12–14] SCs emerge as a promising alternative, characterized by outstanding electrochemical reversibility, minimal thermal output, rapid charge–discharge capability, and extraordinary cycling stability, often exceeding 10^5 cycles.[15,16] SCs exhibit notable increases in energy and power densities due to their improved electrode–electrolyte interfacial characteristics and superior ion transport kinetics, which make them ideal for dynamic energy applications requiring responsiveness and reliability.[17,18] Their robust operational stability, wide electrochemical window, and prolonged cycle life render them highly suitable for high-demand scenarios where performance, endurance, and fast energy delivery are critical.[19] Because of these qualities, SCs are now at the forefront of energy solutions for a variety of applications, such as heavy-duty transportation, grid load balancing, regenerative braking systems, portable electronics, hybrid electric cars, and industrial-scale power management infrastructures.[13,20–24] The integration of organic materials into electronic devices significantly influences the structural and electrochemical behavior of electrode architectures. Among these, porous organic functional materials have emerged as a compelling class of next-generation candidates for energy storage and flexible electronics, owing to their structural tunability and multifunctionality.[25,26] Several critical attributes position porous organic materials as highly attractive for electrochemical applications: (i) they are cost-effective and exhibit favorable photoelectrical properties;[27] (ii) their electrochemical characteristics are inherently stable yet tunable, enabling systematic molecular engineering to optimize charge storage capacities and redox potentials;[28] (iii) their high microporosity offers abundant electroactive sites and enhances ion/electron transport pathways at the electrode–electrolyte interface;[29,30] and (iv) their intrinsic porosity, cross-linked polymeric networks, and diverse functional groups provide broad opportunities for chemical functionalization and performance enhancement.[31,32] Within this material class, CMPs have garnered particular attention due to their π-conjugated frameworks, permanent porosity, and chemically tunable backbones.[33–36] These features confer CMPs with outstanding redox activity, structural diversity, and robust chemical and thermal stability—critical parameters for high-performance energy storage systems.[37,38] The extensive microporous network intrinsic to CMPs facilitates a high density of accessible surface sites, promoting efficient charge transport and ion accessibility. Consequently, CMPs stand at the forefront of advanced organic electrode materials, demonstrating great promise for applications in next-generation flexible and intelligent electronic devices.[39–51] Anthracene (AN), a rigid polycyclic aromatic hydrocarbon characterized by an extended π-conjugated framework, exhibits strong fluorescence and high optical absorbance, making it a cornerstone in a variety of optoelectronic applications. Functionalized anthracene derivatives have been extensively employed in organic light-emitting diodes (OLEDs), fluorescent sensors, electrochromic systems, and dye-sensitized solar cells, owing to their excellent photophysical properties and structural versatility.[52,53] While AN-based motifs have also been explored in battery technologies, their direct integration into SC architectures has remained largely unexplored, primarily due to their intrinsically large energy gaps, which limit electronic conductivity and redox accessibility.[54,55] TzTz scaffolds have garnered significant attention across diverse research domains owing to their rigid, coplanar architecture, extended π-conjugation, and intrinsic electron-deficient nature enriched with nitrogen and sulfur heteroatoms. These molecular features endow TzTz derivatives with exceptional charge transport characteristics and robust environmental stability.[56,57] As a result, TzTz-based compounds have been widely exploited in high-performance applications, including gas separation, organic electronics, and photovoltaics.[58,59] The inherent structural robustness of CMPs enables precise modulation of their electronic properties through heteroatom incorporation, thereby enhancing their electrical conductivity and electrochemical performance. In particular, the strategic integration of donor–acceptor (D–A) moieties facilitates effective band gap engineering, driven by strong intramolecular electronic interactions. This electronic synergy not only lowers the redox potential but also significantly augments the power density, underscoring the potential of D–A-functionalized CMPs in high-performance energy storage and conversion applications.[60] Despite the promising attributes of thiazolo[5,4-*d*]thiazole (TzTz) units, their incorporation into CMPs for energy storage applications remains largely underexplored. To date, only a limited number of studies have reported the construction of TzTz-based donor–acceptor (D–A) CMPs. In a notable advancement, a novel class of (D–A) CMPs was synthesized by coupling electron-rich anthracene (AN) and anthraquinone (ANT)-based aldehydes (ANPh-6CHO and ANTPh-4CHO) with the electron-deficient TzTz *via* a condensation reaction with dithiooxamide, yielding ANPh-TzTz and ANTPh-TzTz CMPs, respectively. Electrochemical characterization demonstrates that ANPh-TzTz CMP exhibits an outstanding specific capacitance of 541 F g^{-1}, coupled with excellent cycling stability, retaining 94% of its capacitance over prolonged operation. Moreover, symmetric coin cell devices assembled with ANPh-TzTz CMP as the active electrode material deliver remarkable energy storage performance, achieving a high energy density of 16.1 Wh kg^{-1} at a power density of 705.9 W kg^{-1}, and a device-level capacitance of 220 F g^{-1}, highlighting its potential for use in future electrochemical energy storage systems.

Experimental section

Materials

4-Formylphenylboronic acid (PFPBA, 98%), anthracene (AN, 97%), cesium carbonate (Cs_2CO_3, ≥99.5%), anthraquinone (ANT, 97%), and dithiooxamide (98%) were obtained from Sigma-Aldrich.

Triphenylphosphine (PPh_3), bromine solution (Br_2, 99%), carbon tetrabromide (CBr_4, 99%), and potassium carbonate

(K_2CO_3, ≥99.8%) were purchased from SHOWA, and tetrakis(triphenylphosphine)palladium [$Pd(PPh_3)_4$, 98%] from Leyan. Dichloromethane (DCM), 1,4-dioxane (DO), toluene, and *N*,*N*-dimethylformamide (DMF) were acquired from Fisher Chemical.

Synthesis of ANPh-6CHO

AN (2.66 g, 15.1 mmol), Br_2 (5.49 g, 100.4 mmol), and Fe powder (5.62 g, 100.4 mmol) were stirred in dry DCM (30 mL) under Ar at RT for 6 h. After quenching with 10% $Na_2S_2O_3$, the solid was washed with DCM, brine, water, and MeOH to give AN-6Br as a gray powder (6.83 g, Scheme S1(a)).[61] A mixture of AN-6Br (1.77 g, 2.66 mmol), PFPBA (4.1 g, 27.33 mmol), K_2CO_3 (3.8 g, 27.4 mmol), and $Pd(PPh_3)_4$ (0.63 g, 0.55 mmol) was placed under vacuum and purged with argon. To the mixture, DO (140 mL), and deionized water (40 mL) were added. For 72 hours, the reaction mixture was heated to 90 °C and vigorously stirred. After completion, the mixture was transferred to ice-cold water containing 2 mL of concentrated HCl. The resulting green solid [ANPh-6CHO] was collected through filtration and washed thoroughly with water to afford the desired product (Scheme S1(b)). FTIR: 2815 and 2731 cm^{-1} (HC═O), 1701 cm^{-1} (C═O) and 3054 cm^{-1}. (Fig. S1). ^{1}HNMR: (500 MHz, DMSO, δ, ppm) 10.15 (2H, CHO), 9.92 (4H, CHO), 8.19, 7.75, 7.68, and 7.31 (Fig. S2). ^{13}CNMR: (125 MHz, δ, ppm) 193 (CHO), 148-126.04 for aromatic carbons (Fig. S3).

Synthesis of ANTPh-4CHO

To a 250 mL flame-dried round-bottomed flask equipped with a magnetic stir bar were added ANT (3.67 g, 17.63 mmol), CBr_4 (23.4 g, 70.5 mmol), and PPh_3 (30.9 g, 141 mmol) in 100 mL of anhydrous toluene under an inert atmosphere. The resulting mixture was heated at reflux (115 °C) for 72 h. Using dichloromethane/hexane (1 : 4 v/v) as the eluent, the reaction mixture was cooled to room temperature, concentrated under reduced pressure, and the crude product was purified by flash column chromatography on silica gel. The extracted white solid was recrystallized from methanol to afford pure 9,10-bis(dibromomethylene)-9,10-dihydroanthracene (ANT-4Br) as white crystalline needles [Scheme S2(a)]. In a 100 mL oven-dried round-bottomed flask, ANT-4Br (1.15 g, 2.21 mmol), PFPBA (3.1 g, 13.34 mmol), Cs_2CO_3 (11.5 g, 35.31 mmol), and $Pd(PPh_3)_4$ (03 g, 0.22 mmol) were suspended in a biphasic mixture of DO (100 mL) and deionized water (40 mL). For 16 h, the reaction mixture was heated to reflux under vigorous stirring. After cooling to ambient temperature, the reaction was quenched with brine and extracted with DCM (2 × 50 mL). After being dried over anhydrous $MgSO_4$, the mixed organic layers were filtered and vacuum concentrated. Purification by silica gel chromatography using hexanes/ethyl acetate (4 : 6 v/v) furnished ANTPh-4CHO as a pale yellow solid (1.2 g, Scheme S2(b)). FTIR (cm^{-1}, Fig. S4): 3062, 2834, 2740, 1703 cm^{-1}. ^{1}H NMR (500 MHz, DMSO-d_6): δ 9.98 (s, 4H), 7.94, 7.87, 6.96, 6.81 ppm [Fig. S5]. ^{13}C NMR (500 MHz, DMSO-d_6): δ 193 (CHO), 147.51–126.04 ppm [Fig. S6].

Synthesis of ANPh-TzTz CMP and ANTPh-TzTz CMP

In a typical synthesis of ANPh-TzTz CMP and ANTPh-TzTz CMP, a 100 mL Schlenk tube was charged under argon with dithiooxamide (0.22 g, 1.9 mmol) and ANPh-6CHO (0.5 g, 0.62 mmol) or ANTPh-4CHO (0.57 g, 0.91 mmol). Dry DMF (45 mL) was added, and the reaction mixture was stirred at 135 °C for 180 h. After cooling to room temperature, the dark brown precipitate was collected through filtration and then refined by Soxhlet extraction using DMF to remove unreacted monomers and low-molecular-weight byproducts. The CMP yielded the ANPh-TzTz CMP as a fine dark green powder [Scheme S3] and the ANTPh-TzTz CMP as a dark brown solid [Scheme S4].

Results and discussion

Synthesis and structural characterization of ANPh-TzTz CMP and ANTPh-TzTz CMP

Two conjugated microporous polymers (CMPs), namely ANPh-TzTz CMP and ANTPh-TzTz CMP, were strategically engineered for applications in supercapacitor systems (SCs). These CMPs incorporate anthracene (AN), anthraquinone (ANT), and the electron-deficient thiazolo[5,4-*d*]thiazole (TzTz) units, as illustrated in Scheme 1(c) and (d). ANPh-TzTz CMP [Scheme 1(c)] was obtained as a vibrant green powder through the reaction of ANPh-6CHO [Scheme 1(a)] with dithioxamide, while ANTPh-TzTz CMP [Scheme 1(d)] was obtained as a distinct deep-brown solid prepared by the reaction of ANTPh-4CHO [Scheme 1(b)] with dithioxamide. These pronounced color differences stem from the incorporation of heteroatoms (S/N) and the extended π-conjugation frameworks. Remarkably, both CMPs [ANPh-TzTz CMP and ANTPh-TzTz CMP] exhibit exceptional chemical stability in aqueous environments and are completely insoluble in a broad range of common organic solvents [DMSO, DMF, THF, and DCM], underscoring their robust structural integrity. The key aldehyde-functionalized monomers, ANPh-6CHO and ANTPh-4CHO, were synthesized *via* a robust Suzuki–Miyaura cross-coupling reaction between AN-6Br or ANT-4Br and 4-formylphenylboronic acid (PFPBA), serving as the aldehyde source. This efficient transformation yielded ANPh-6CHO as a green powder [Scheme S1] and ANTPh-4CHO as a white powder [Scheme S2], as shown in the Experimental section. FTIR and NMR spectroscopy unambiguously confirmed the molecular structures of ANPh-6CHO and ANTPh-4CHO, respectively. As depicted in Fig. S1 and S4, the FTIR spectrum of ANPh-6CHO [Fig. S1] exhibits distinct absorption bands corresponding to the aldehyde C–H stretches at 2815 and 2731 cm^{-1}, the aromatic sp^2 C–H stretch at 3054 cm^{-1}, and a strong C═O stretching vibration at 1701 cm^{-1}. In the case of ANTPh-4CHO [Fig. S4], the FTIR spectrum displays well-defined absorption bands attributable to the aldehyde C–H stretches at 2834 and 2740 cm^{-1}, the aromatic C–H vibration at 3062 cm^{-1}, and a prominent C═O stretching band at 1703 cm^{-1}. The ^{1}H NMR spectra of ANPh-6CHO (Fig. S2) and ANTPh-4CHO (Fig. S5) further corroborate their structures, each exhibiting a pronounced downfield resonance characteristic of the aldehydic proton. ANPh-6CHO shows distinct signals at 10.15 and 9.92 ppm, while ANTPh-4CHO displays a sharp aldehyde peak at 9.98 ppm, definitively confirming the presence of the formyl functionality in both monomers. Furthermore, the existence of carbonyl functionalities was strongly supported by ^{13}C NMR

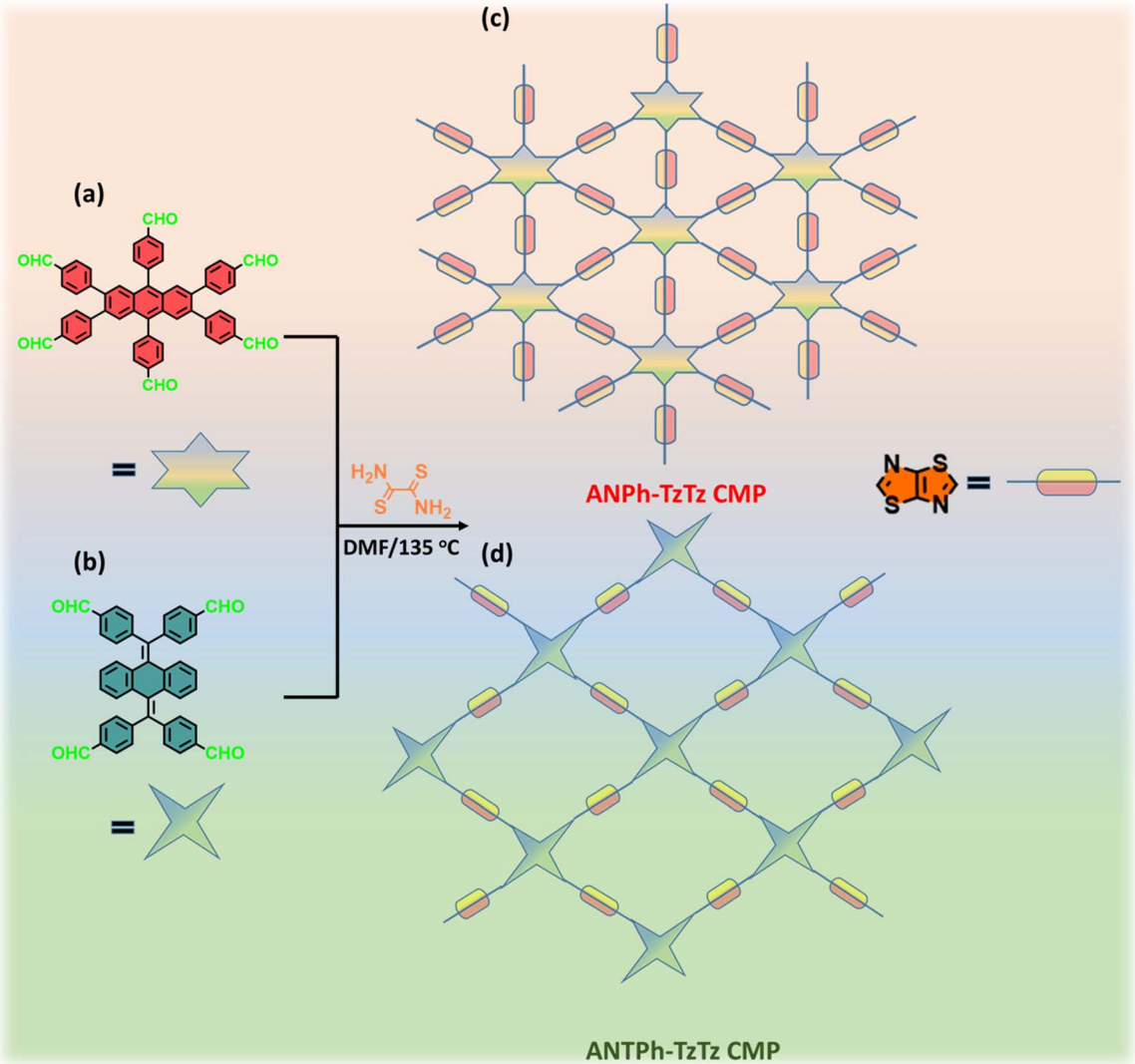

Scheme 1 Synthesis process of (c) ANPh-TzTz CMP and (d) ANTPh-TzTz CMP from (a) ANPh-6CHO and (b) ANTPh-4CHO and dithiooxamide.

analysis, which showed distinctive C=O resonances for both ANPh-6CHO (Fig. S3) and ANTPh-4CHO (Fig. S6), at about 193 ppm, further validating the successful incorporation of the aldehyde groups. The successful synthesis of ANPh-TzTz CMP and ANTPh-TzTz CMP was unambiguously confirmed through solid-state ^{13}C CPMAS NMR and FT-IR spectroscopy. In the FT-IR spectra [Fig. 1(a)], characteristic absorption bands observed near 3059–3049 cm^{-1}, 1675–1657 cm^{-1}, and 835–826 cm^{-1} provide compelling evidence for the incorporation of aromatic sp^2 C–H moieties from the AN and ANT units, as well as the presence of C=N and C–S–C functionalities, which are diagnostic of the TzTz framework. The ^{13}C CPMAS NMR spectra of ANPh-TzTz CMP and ANTPh-TzTz CMP [Fig. 1(b)] exhibit no substantial differences, reflecting their closely related molecular architectures. A prominent resonance peak at approximately 169 ppm is attributed to the N=C carbon of the TzTz moiety conjugated to the aromatic backbone, while the weaker signal near 150 ppm corresponds to the aromatic carbon directly bonded to the TzTz unit. Broad resonances spanning 138 to 127 ppm are indicative of the diverse aromatic carbon environments within the CMP network, underscoring the extended π-conjugated structure.[62] Thermogravimetric analysis (TGA) was conducted to evaluate the thermal resilience and char yield of ANPh-TzTz CMP and ANTPh-TzTz CMP. The materials exhibited substantial carbon residues of 66 wt% and 61 wt% at 800 °C, reflecting their excellent thermal durability. The T_{d10} values—defined as the temperature at which 10% weight loss occurs—were measured at 435 °C for ANPh-TzTz CMP and 246 °C for ANTPh-TzTz CMP [Fig. 1(c)]. The structural features of both ANPh-TzTz and ANTPh-TzTz CMPs were rigorously examined *via* powder X-ray diffraction (XRD) using Cu Kα radiation over a 2θ range of 3–60°. Both materials exhibited a broad diffraction halo centered around 2$\theta \approx 19°$, indicative of their predominantly amorphous nature [Fig. 1(d)]. The lack of long-range order in these amorphous frameworks confers distinct electrochemical advantages over crystalline analogs. Specifically, the abundance of coordinatively unsaturated sites and structural defects facilitates enhanced charge transport and ion

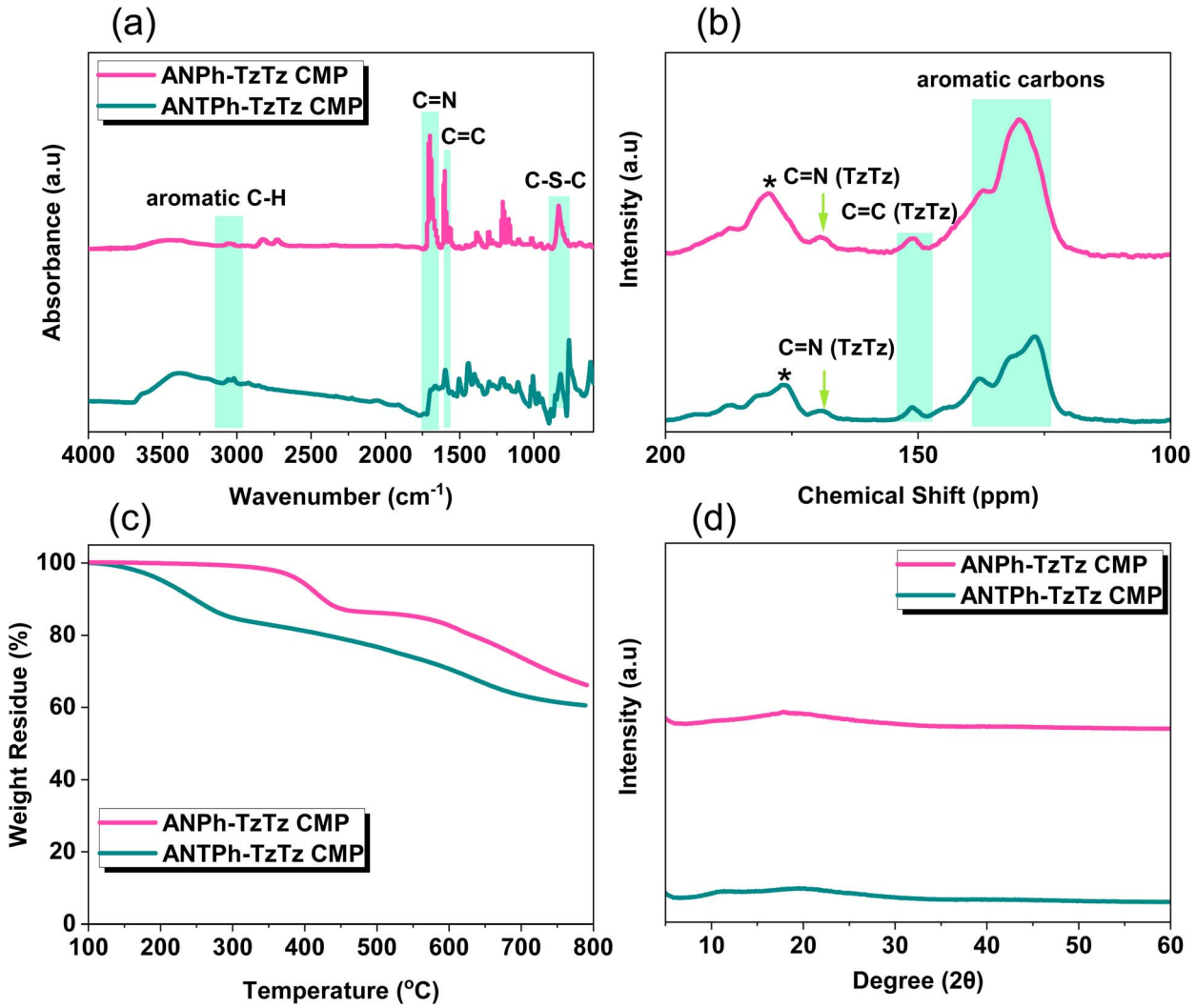

Fig. 1 (a) FTIR, (b) solid state ^{13}C-NMR, (c) TGA, and (d) XRD analyses of ANPh-TzTz CMP and ANTPh-TzTz CMP.

diffusion.[63] Moreover, the inherent disorder imparts flexibility to the framework, enabling adaptive self-reconstruction during cycling, thereby promoting both rapid reaction kinetics and long-term structural stability. The elemental composition of the ANPh-TzTz and ANTPh-TzTz CMPs was further elucidated through X-ray photoelectron spectroscopy (XPS) [Fig. S7]. The survey spectrum confirmed the presence of carbon (C), nitrogen (N), and sulfur (S) in both frameworks. Quantitative analysis revealed atomic weight percentages of 67.8% C, 22.7% N, and 9.3% S for ANPh-TzTz CMP, whereas ANTPh-TzTz CMP comprised 68.9% C, 21.7% N, and 9.2% S (Table S1). Deconvolution of high-resolution C 1s spectra identified peaks corresponding to C=C at 283.6 eV (ANPh-TzTz CMP) [Fig. 2(a)] and 283.5 eV (ANTPh-TzTz CMP) [Fig. 2(d)]. In contrast, signals at 284.6 and 284.4 eV were attributed to C–N/C=N linkages. Distinct C–S contributions were observed at 289.6 eV and 288.9 eV for ANPh-TzTz and ANPh-TzTz CMPs, respectively. The N 1s spectra revealed peaks at 399.6 and 401.0 eV, assigned to N–C and N=C in ANPh-TzTz CMP [Fig. 2(b)], with analogous peaks at 399.5 and 400.1 eV in ANTPh-TzTz CMP [Fig. 2(e)]. For S 2p, characteristic doublets at 163.7 and 167.3 eV (ANPh-TzTz CMP) [Fig. 2(c)] and 163.5 and 165.6 eV (ANTPh-TzTz) [Fig. 2(f)] correspond to S $2p_{3/2}$ and S $2p_{1/2}$ states. The relative abundance of each functional group was determined from the integrated areas of the deconvoluted peaks (Table S2). The N_2 sorption isotherms of ANPh-TzTz and ANTP-TzTz CMP correspond to type IV behavior with H4-type hysteresis, indicating a micro–mesoporous texture. The steep uptake at $P/P_0 < 0.1$ evidences significant microporosity, while the hysteresis loop suggests the presence of slit-like mesopores or interparticle voids [Fig. 3(a) and (b)], characteristic of microporous architectures. The Brunauer–Emmett–Teller (BET) surface areas (S_{BET}) were measured to be 213 $m^2\ g^{-1}$ for ANPh-TzTz CMP and 115 $m^2\ g^{-1}$ for ANTPh-TzTz CMP. The total pore volumes (TPVs) of ANPh-TzTz and ANTPh-TzTz CMPs were 0.19 and 0.40 $cm^3\ g^{-1}$, respectively.

Pore size diameters (PSD), determined using the non-local density functional theory (NLDFT) model, were 1.86 nm for ANPh-TzTz CMP [Fig. 3(c)] and ranged from 1.06 to 2.31 nm for ANTPh-TzTz CMP [Fig. 3(d)]. Quantitative analysis confirmed this

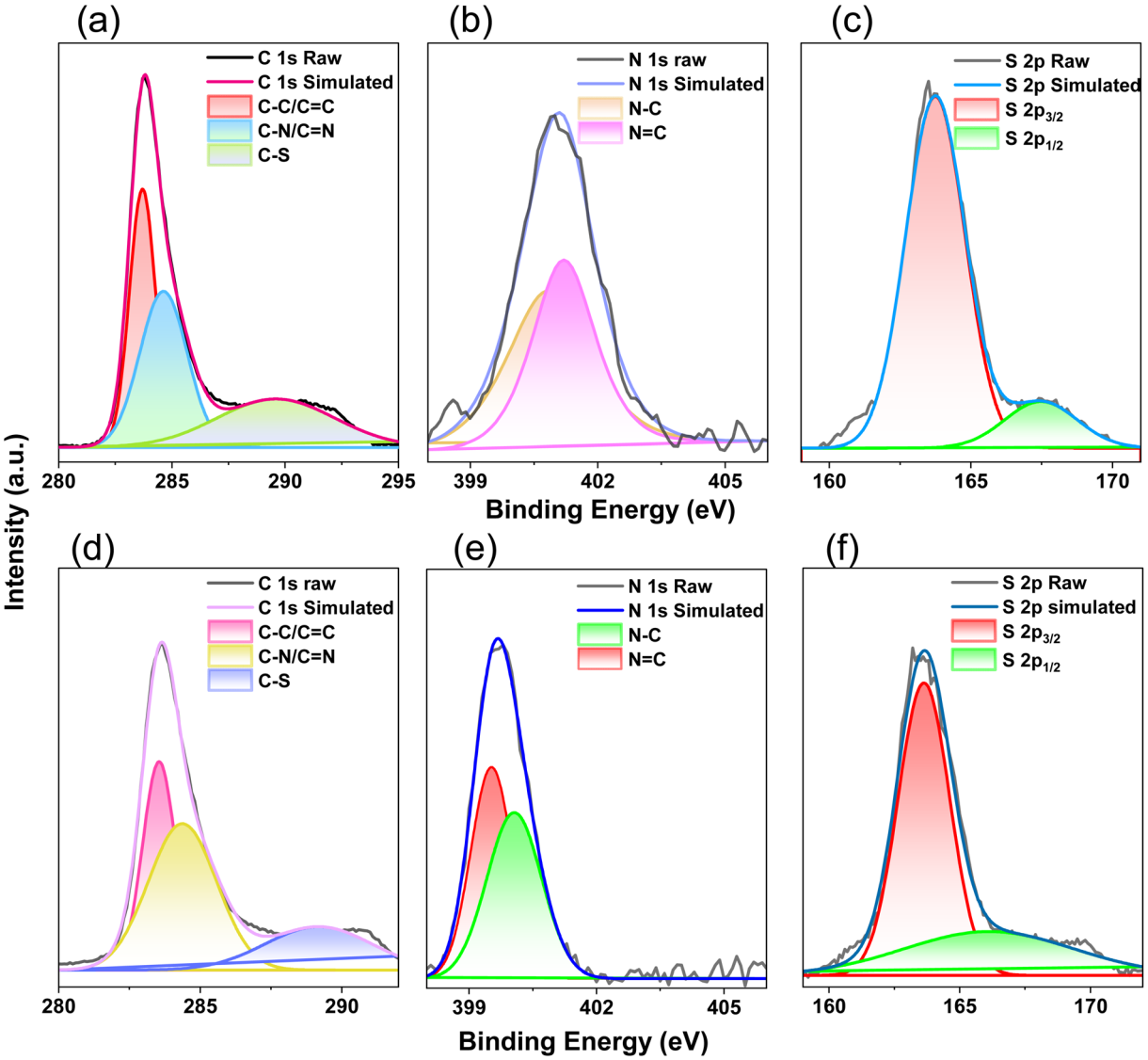

Fig. 2 High-resolution XPS spectra and corresponding peak fittings of (a and d) C 1s, (b and e) N 1s, and (c and f) S 2p for (a–c) ANPh-TzTz CMP and (d–f) ANTPh-TzTz CMP.

dual porosity; t-plot analysis (Fig. S8) revealed a micropore volume of 0.233 $cm^3\ g^{-1}$ for ANPh-TzTz, which constitutes approximately 58.3% of its total pore volume (0.4 $cm^3\ g^{-1}$). The majority of the pore volume is attributed to micropores, aligning with the observed isotherm shape. ANTPh-TzTz displays a similar micro–mesoporous character, albeit with a lower overall pore volume ($V_{total} = 0.19\ cm^3\ g^{-1}$; $V_{micro} = 0.0103\ cm^3\ g^{-1}$) (Table S3). These variations in porosity metrics are attributed to subtle differences in molecular architecture and packing behavior. Transmission electron microscopy (TEM) images [Fig. 3(e–h)] further corroborate the disordered morphology; no lattice fringes were observed even at high magnification, reinforcing the amorphous character of the ANPh-TzTz CMP and ANTPh-TzTz CMP. Notably, this disordered yet porous framework supports facile electrolyte penetration and ion transport during high-rate electrochemical cycling, a key attribute for advanced energy storage applications. Morphological characterization by scanning electron microscopy (SEM) revealed that ANPh-TzTz CMP exhibits a more rod-like morphology [Fig. 3(i)] while ANTPh-TzTz CMP displays irregularly aggregated, amorphous particles[Fig. 3(j)]. Elemental mapping *via* SEM-EDS confirmed the uniform distribution of C, N, and S within both the ANPh-TzTz CMP and ANTPh-TzTz CMP [Fig. S9].

Electrochemical performance of ANPh-TzTz and ANTPh-TzTz CMPs based on three-electrode systems

The electrochemical performance of ANPh-TzTz and ANTPh-TzTz CMPs was systematically investigated using cyclic voltammetry (CV) and galvanostatic charge–discharge (GCD) measurements in a three-electrode configuration with 1 M KOH as the electrolyte. ANPh-TzTz and ANTPh-TzTz CMPs served as active electrode materials, with a Pt wire and Hg/HgO employed as counter and reference electrodes, respectively. A slurry was prepared by dispersing the ANPh-TzTz and ANTPh-TzTz CMPs (50%), carbon

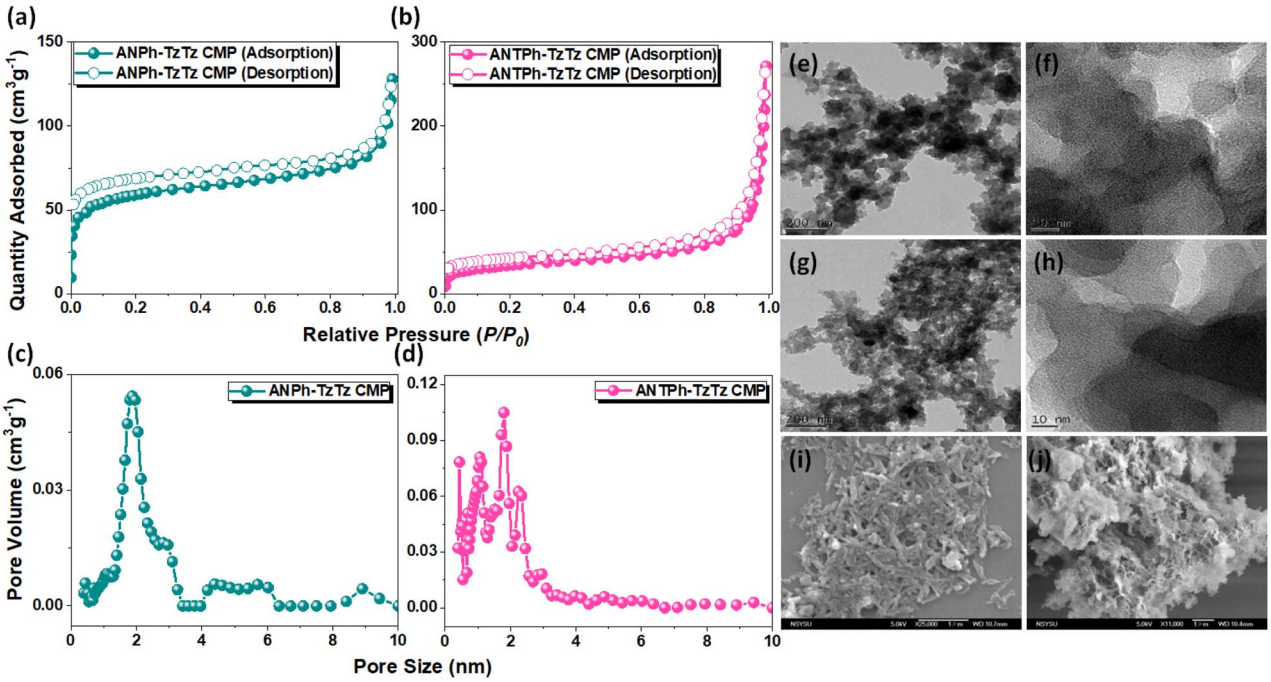

Fig. 3 (a and b) N_2 adsorption–desorption isotherms, (c and d) pore size diameters, (e–h) TEM images, and (i and j) SEM images for (a, c, e, f and i) ANPh-TzTz CMP and (b, d, g–j) ANTPh-TzTz CMP.

black (CB, 40%), and Nafion (10%) in a mixture of EtOH/H_2O (200 μL: 800 μL) and then sonicated for 2 h. CV experiments were conducted over a potential window of −1.0 to 0 V at scan rates ranging from 5 to 20 mV s^{-1} [Fig. 4(a) and (c)]. Both ANPh-TzTz and ANTPh-TzTz CMPs exhibited nearly rectangular CV profiles, indicative of dominant electric double-layer capacitance (EDLC) behavior. Minor deviations from ideal rectangularity suggest a pseudocapacitive contribution, likely arising from redox-active moieties embedded within the framework.[64,65] GCD measurements [Fig. 4(b) and (d)], performed over the same potential window at current densities ranging from 1 to 20 A g^{-1}, revealed that both ANTPh-TzTz and ANPh-TzTz CMPs have symmetric triangular profiles without discernible redox plateaus, consistent with capacitive energy storage.

At low scan rates, higher specific capacitance was observed, suggesting efficient electrolyte ion diffusion and access to internal active sites. Conversely, a marked decline in capacitance at higher current densities reflects kinetic limitations in ion transport, restricting charge storage to external surfaces. Specific capacitances calculated from GCD data reached 356 F g^{-1} for ANTPh-TzTz CMP and an impressive 541 F g^{-1} for ANPh-TzTz CMP at 1 A g^{-1} [Fig. 5(a)]. Both materials exhibited rapid capacitance decay with increasing current density, attributed to diffusion constraints within the porous matrix. Furthermore, the specific capacitances of the ANPh-TzTz CMP and ANTPh-TzTz CMP, determined from GCD measurements at a current density of 1 A g^{-1} [Fig. S10(a) and (b)], were evaluated after incorporating 10 wt% and 20 wt% of carbon black. The results demonstrate that, with 10 wt% carbon black, the specific capacitances reached 431 F g^{-1} for ANPh-TzTz CMP and 322 F g^{-1} for ANTPh-TzTz CMP at 1 A g^{-1}. When the carbon black content was increased to 20 wt%, the capacitances further improved to 473 F g^{-1} and 340 F g^{-1}a respectively, at 1 A g^{-1}, as illustrated in Fig. S10(c). Long-term cycling stability assessed over 5000 charge–discharge cycles demonstrated excellent retention of 94% and 93% for ANPh-TzTz CMP and ANTPh-TzTz CMP, respectively [Fig. 5(b)], underscoring the structural robustness and electrochemical durability of the TzTz-linked CMP networks. The presence of TzTz moieties contributes significantly to charge storage by introducing nitrogen-rich sites that enhance electrical conductivity, stabilize the framework, and increase the density of electroactive centers.[66] Further insight into the charge storage mechanism was obtained *via* power-law analysis (eqn (1)), providing a quantitative evaluation of capacitive *versus* diffusion-controlled contributions.

$$i = av^b \quad (1)$$

The power-law equation was used to examine the relationship between peak current (i) and scan rate (v) to clarify the underlying charge storage behavior, where a and b are adjustable parameters and b represents the slope obtained from log(i) *vs.* log(v) plots [Fig. 6(a) and (b)]. The charge storage mechanism is diagnostically indicated by the value of b, where $b \approx 0.5$ signifies diffusion-controlled processes and $b \approx 1$ corresponds to capacitive-dominated behaviour.[67,68] The calculated b-values were 0.89 for ANTPh-TzTz CMP and 1.01 for ANPh-TzTz CMP, suggesting a predominantly capacitive response in both systems, with ANPh-TzTz CMP exhibiting nearly ideal surface-controlled kinetics. Further quantitative analysis of capacitive *versus* diffusion-controlled contributions was carried out using eqn (2), and the results are presented in [Fig. 6(c) and (d)].

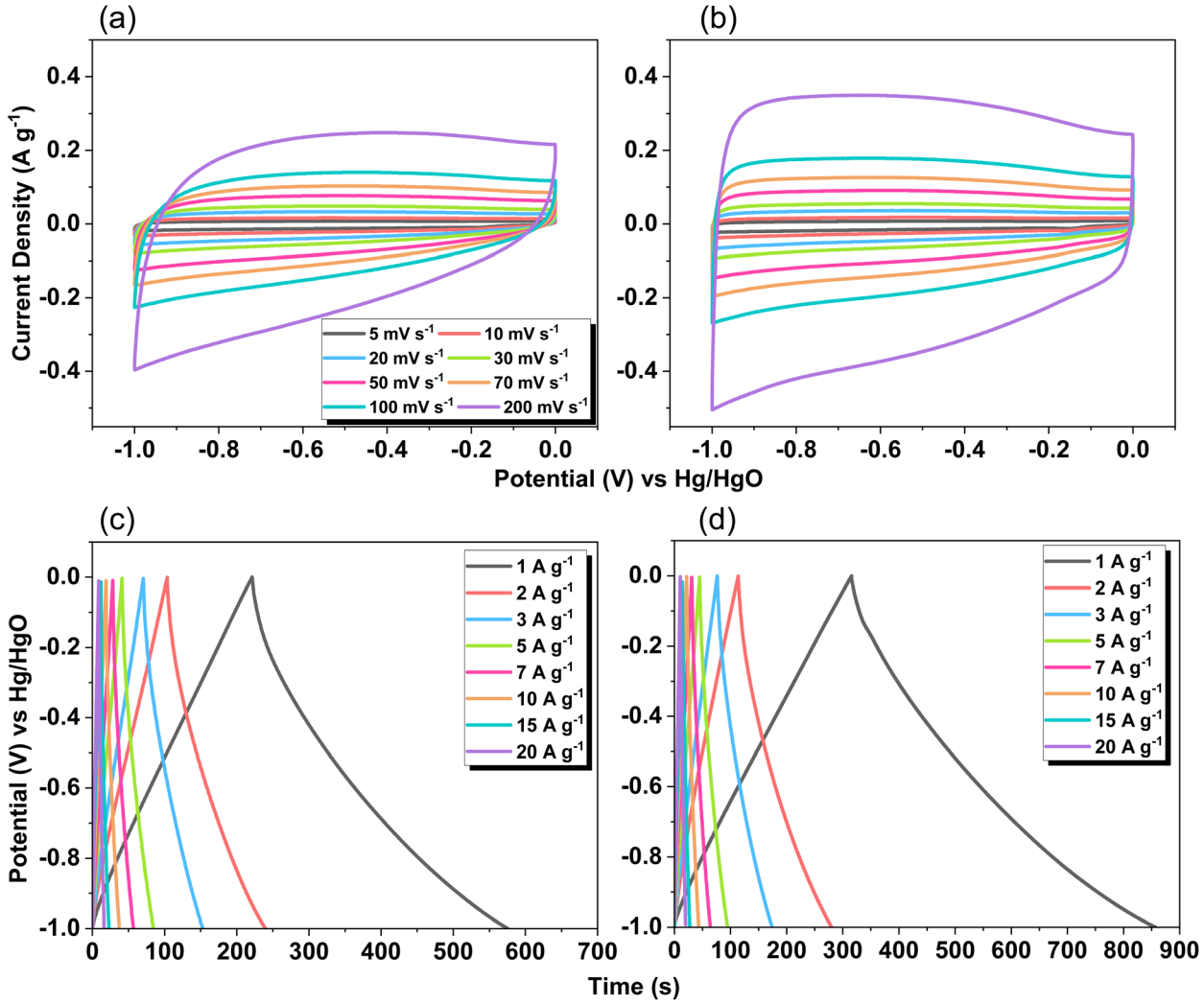

Fig. 4 (a and b) CV and (c and d) GCD of (a–c) ANTPh-TzTz CMP and (b and d) ANPh-TzTz CMP, measured using a three-electrode setup.

$$i(V) = k_1 v + k_2 v^{1/2} \quad (2)$$

At a scan rate of 5 mV s^{-1}, surface-controlled charge storage accounted for 91% and 81% of the total current response in ANTPh-TzTz CMP and ANPh-TzTz CMP, respectively. Notably, these contributions increased significantly at higher scan rates (20 mV s^{-1}), reaching 98% for ANTPh-TzTz CMP and 99% for ANPh-TzTz CMP. This trend strongly supports the dominance of surface-confined capacitive behavior under fast charge–discharge conditions, attributed to limited ion diffusion into the porous network at higher scan rates. These findings corroborate the efficient electrochemical accessibility of active sites and the fast surface redox kinetics conferred by the TzTz-linked CMP architecture.

Electrochemical performance of the symmetric coin cell of ANTPh-TzTz and ANPh-TzTz CMPs

CV and GCD measurements were conducted on symmetric devices fabricated with ANTPh-TzTz CMP and ANPh-TzTz CMP electrodes over an extended window of positive potential from 0 to +0.7 V. As shown in Fig. 7, the CV profiles of ANTPh-TzTz and ANPh-TzTz CMPs exhibit nearly ideal rectangular shapes at lower potentials, indicative of pronounced electric double-layer capacitance (EDLC) behavior [Fig. 7(a) and (b)].

Notably, a clear pseudocapacitive contribution is also apparent, highlighting the synergistic interplay between EDLC and faradaic charge storage processes. Remarkably, the electrode responses remain stable even at elevated scan rates, underscoring their excellent electrochemical reversibility and superior rate capability. The GCD curves [Fig. 7(c) and (d)] further corroborate this behavior, displaying symmetric and linear charge–discharge profiles characteristic of EDLC-dominated mechanisms. At 1 A g^{-1}, the ANTPh-TzTz CMP and ANPh-TzTz CMP exhibit specific capacitances of 138 and 220 F g^{-1}, respectively [Fig. 8(a)]. Even at a high current density of 20 A g^{-1}, both electrodes retain appreciable capacitance values (40 and 80 F g^{-1}), demonstrating excellent high-rate performance and structural resilience. The observed decline in capacitance at elevated current densities can be attributed to

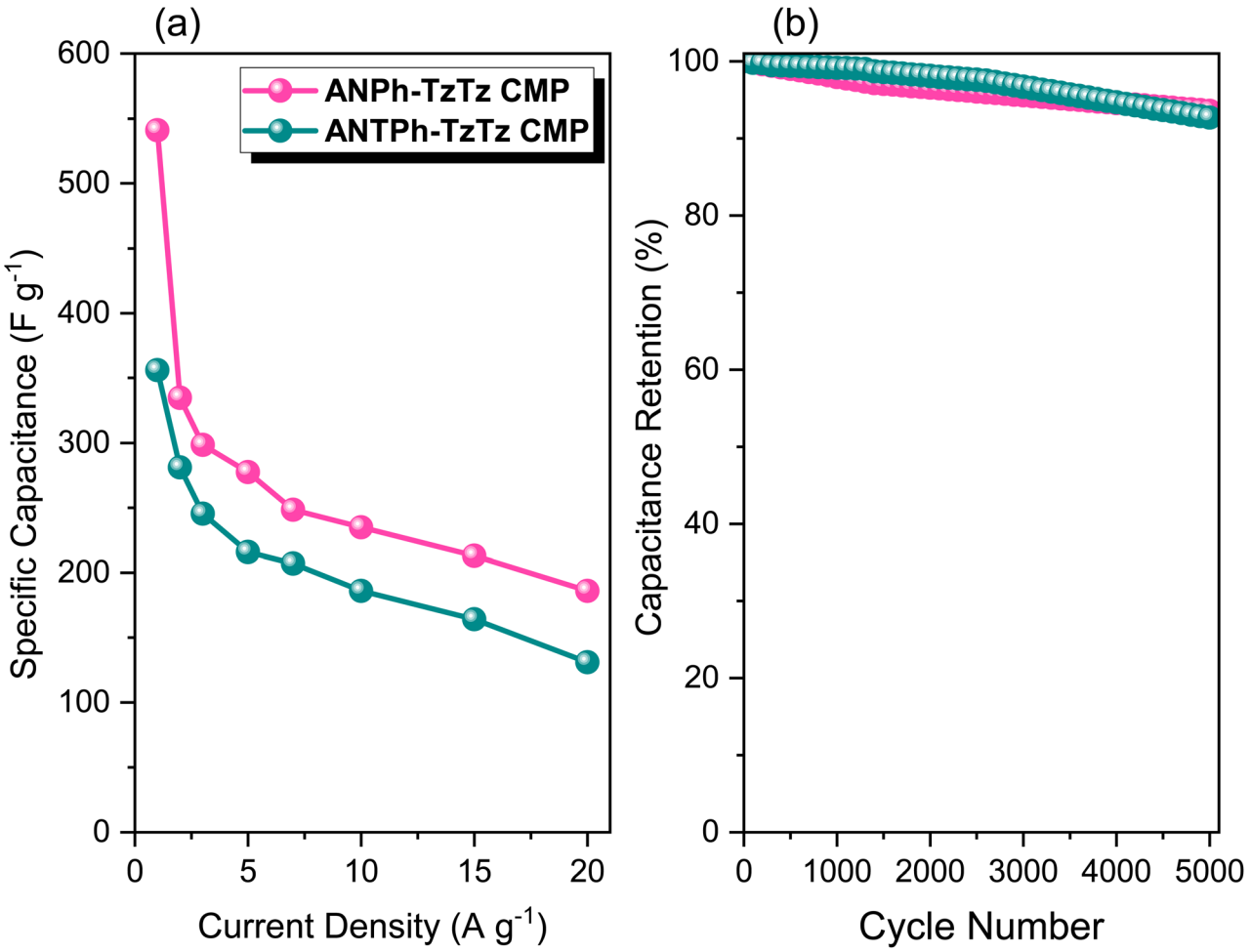

Fig. 5 (a) Specific capacitance and current density graph and (b) percentage capacitance retention of ANPh-TzTz CMP and ANTPh-TzTz CMP, measured using a three-electrode setup.

kinetic limitations, specifically the restricted diffusion of electrolyte ions into the microporous network of the electrodes. This behavior reflects reduced efficiency of ion adsorption/desorption dynamics at high charge–discharge rates. Crucially, the robust electrochemical performance is ascribed to the intrinsic properties of the porous framework and the incorporation of redox-active heteroatoms, particularly sulfur and nitrogen. These heteroatoms endow the materials with enhanced electronic conductivity and a greater density of electrochemically accessible sites.[69,70] Notably, ANPh-TzTz CMP outperforms its analogue, which is rationalized by its higher nitrogen and sulfur content. The cooperative effect of S and N co-doping significantly augments the electrochemical activity by creating abundant redox-active centers, improving charge transfer kinetics, and stabilizing the electrode architecture.[71]

Sulfur contributes by modulating the electronic environment to facilitate charge delocalization, whereas nitrogen enhances conductivity *via* electron donation and improved orbital overlap. Collectively, these features position ANPh-TzTz CMP as a highly promising candidate for next-generation high-performance SCs. Furthermore, their inclusion promotes higher porosity and introduces abundant structural defects, which serve as additional electrochemically active sites for charge storage. These structural benefits lead to remarkable cycling durability, higher rate capability, and a noticeable increase in specific capacitance.[72,73] The increased density of accessible sites enables greater accumulation of electrolyte ions at the interface of electrode–electrolyte, effectively boosting overall charge storage capacity. Simultaneously, the enlarged surface area reduces ion diffusion pathways, thereby facilitating faster ion transport and accelerating charge–discharge kinetics—an essential characteristic for high-performance supercapacitors.[74] This optimized electrode architecture translates into outstanding cycling stability. After 4000 consecutive charge–discharge cycles, ANPh-TzTz and ANTPh-TzTz CMPs retained 95% and 93% of their initial capacitance, respectively [Fig. 8(b)], attesting to their remarkable long-term electrochemical resilience. Such high retention underscores the robustness and reliability of these materials, making them ideal for practical energy storage systems requiring sustained cycling, mechanical integrity, and minimal performance degradation over time. Further insight into the energy–power characteristics of these CMP-based electrodes is provided by the Ragone plot [Fig. 8(c)]. The ANPh-TzTz CMP achieves a notable energy

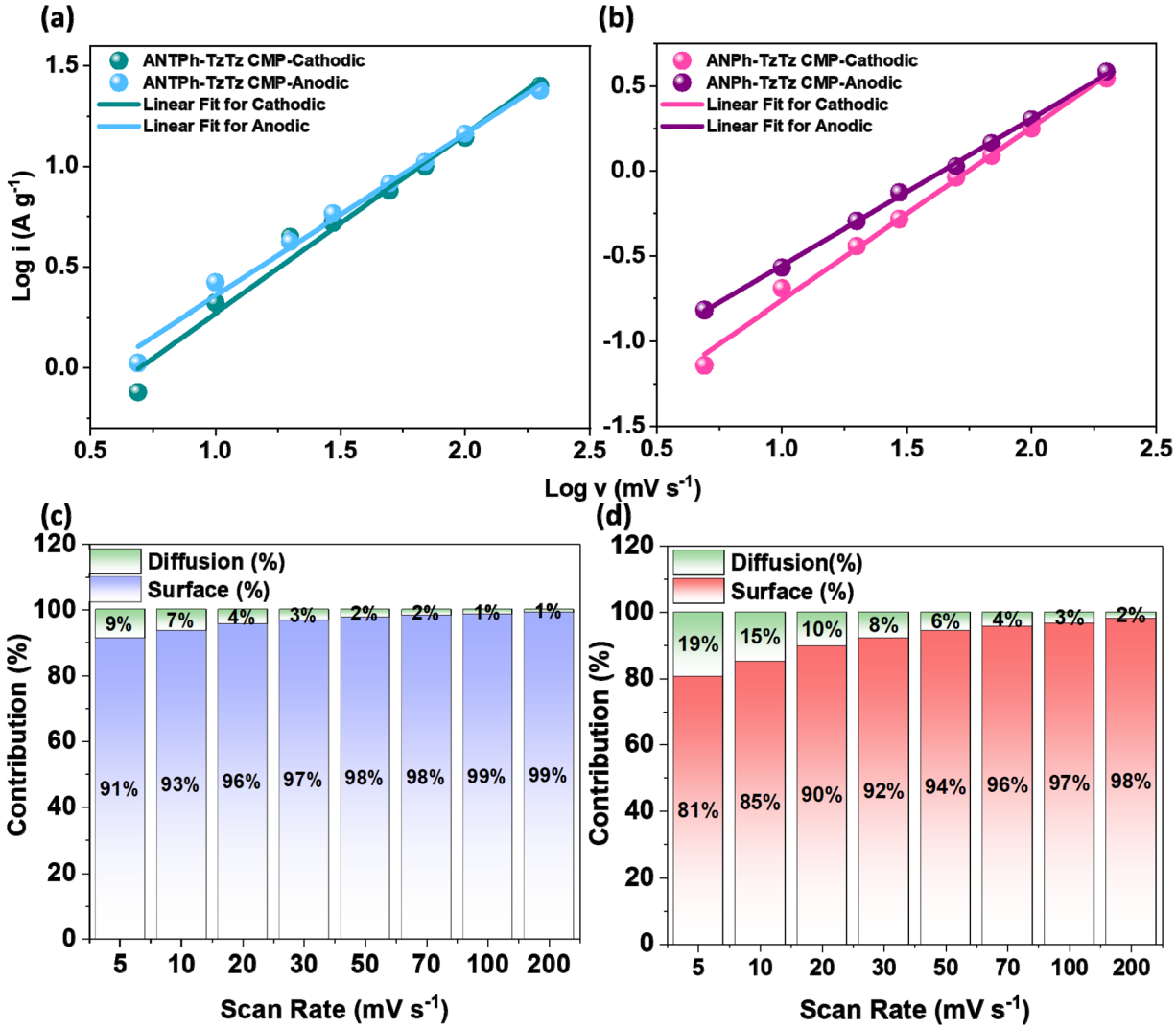

Fig. 6 (a and b) Comparison of charge storage contributions based on log *v vs.* log *i* plots and (c and d) Dunn's method analysis for (a–c) ANTPh-TzTz CMP and (b and d) ANPh-TzTz CMP.

density of 16.1 Wh kg^{-1} at a power density of 705.9 W kg^{-1}, and impressively sustains an ultra-high-power density of 18 981.1 W kg^{-1} at an energy density of 5.8 Wh kg^{-1}. In comparison, the ANTPh-TzTz CMP delivers an energy density of 9.3 Wh kg^{-1} at 730.9 W kg^{-1}.

These metrics position both materials—particularly ANPh-TzTz CMP—as highly competitive candidates for power-oriented energy storage devices, where rapid charge delivery and long-term durability are paramount. A comprehensive performance comparison of these CMPs with state-of-the-art analogs is provided in Fig. 8(d). To elucidate the underlying charge storage mechanisms and the intrinsic electrochemical behavior of the CMP electrodes, both Dunn's method and Trasatti's approach were systematically employed.[75,76] The log–log plots of current (i) *versus* scan rate (v) for anodic and cathodic sweeps [Fig. S11(a) and (b)] yield slope values corresponding to the b-factor, extracted from eqn (2). The b-values determined for ANTPh-TzTz and ANPh-TzTz CMPs are 0.57 and 0.72, respectively, revealing distinct differences in charge storage behavior. Specifically, the higher slope for the ANPh-TzTz CMP suggests a greater contribution from surface-controlled (capacitive) processes, whereas ANTPh-TzTz CMPs demonstrate a more diffusion-dominated mechanism. Fig. S11(c) and (d) provide a quantitative assessment of the capacitive and diffusion-controlled contributions as a function of scan rate for both materials. As anticipated, the restricted diffusion of electrolyte ions into the porous network at a higher scan rate causes the capacitive contribution to become more prominent as scan rates increase. Conversely, at lower scan rates, the pseudocapacitive contribution—attributable to redox-active sulfur and nitrogen heteroatoms embedded within the TzTz moieties—becomes more pronounced, facilitating deeper ion penetration and more complete utilization of active sites. Trasatti's method was also employed to decouple the electric double-layer capacitance (EDLC) and pseudocapacitive contributions. The areal capacitances calculated from CV curves at various scan rates

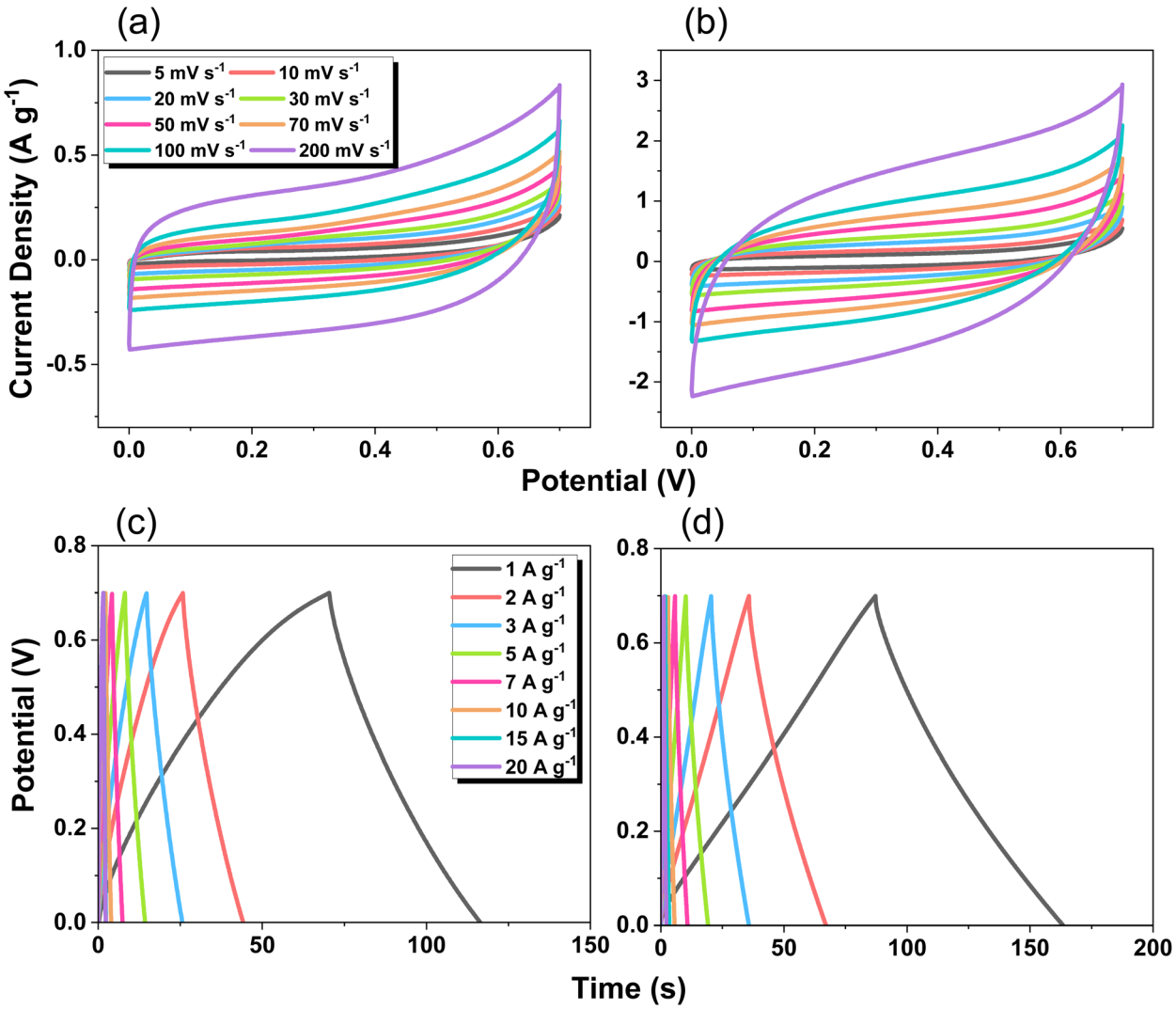

Fig. 7 (a and b) CV and (c and d) GCD of (a and c) ANTPh-TzTz CMP and (b and d) ANPh-TzTz CMP, measured using a symmetric coin cell.

were found to be 251.8 mF cm^{-2} and 564.0 mF cm^{-2} for ANTPh-TzTz and ANPh-TzTz CMPs, respectively [Fig. S12(a)], underscoring the superior capacitive performance of ANPh-TzTz CMPs. A linear relationship observed in the plot of the square root of the scan rate ($v^{1/2}$) *versus* the reciprocal of areal capacitance [Fig. S12(b)] confirms a semi-infinite diffusion process. The *y*-intercept of this linear fit corresponds to the inverse of the EDLC, as defined by eqn (3), enabling the quantitative differentiation between capacitive and diffusion-controlled charge storage components.

$$C^{-1} = \text{constant} \times v^{1/2} + C_t^{-1} \quad (3)$$

Assuming semi-infinite ion diffusion kinetics, a linear relationship is also observed when plotting areal capacitance against the reciprocal square root of the scan rate. The intercept of this linear fit corresponds to the inverse of the total capacitance (C_t), providing a reliable measure of the intrinsic electrochemical behavior. The estimated pseudocapacitive contribution, derived *via* this method, closely parallels that obtained using Dunn's approach, with ANTPh-TzTz and ANPh-TzTz CMPs exhibiting dominant capacitive behavior—92% and 91% surface-controlled contribution, respectively, at a scan rate of 5 mV s^{-1} [Fig. S12(c) and (d)]. These results confirm that EDLC is the dominant mechanism across the scan rate range for both CMPs. To further probe the charge storage dynamics and interfacial properties, electrochemical impedance spectroscopy (EIS) was employed. The Nyquist plots for ANTPh-TzTz and ANPh-TzTz CMPs [Fig. S13(a)] reveal well-defined profiles characteristic of porous carbon-based electrodes. In the high-frequency region, the semicircular arc reflects the solution resistance (R_s) and charge transfer resistance (R_{ct}). In addition, the near-vertical line in the low-frequency domain that is ascribed to Warburg impedance (W) shows that ions diffuse through the porous structure. Non-ideal capacitive behavior, especially at low frequencies, is explained by the constant phase element (CPE), which reflects distributed capacitance caused by pore distribution and surface heterogeneity. Fitting of the impedance spectra yields R_s values of 10.5 and 7.5 Ω and R_{ct}

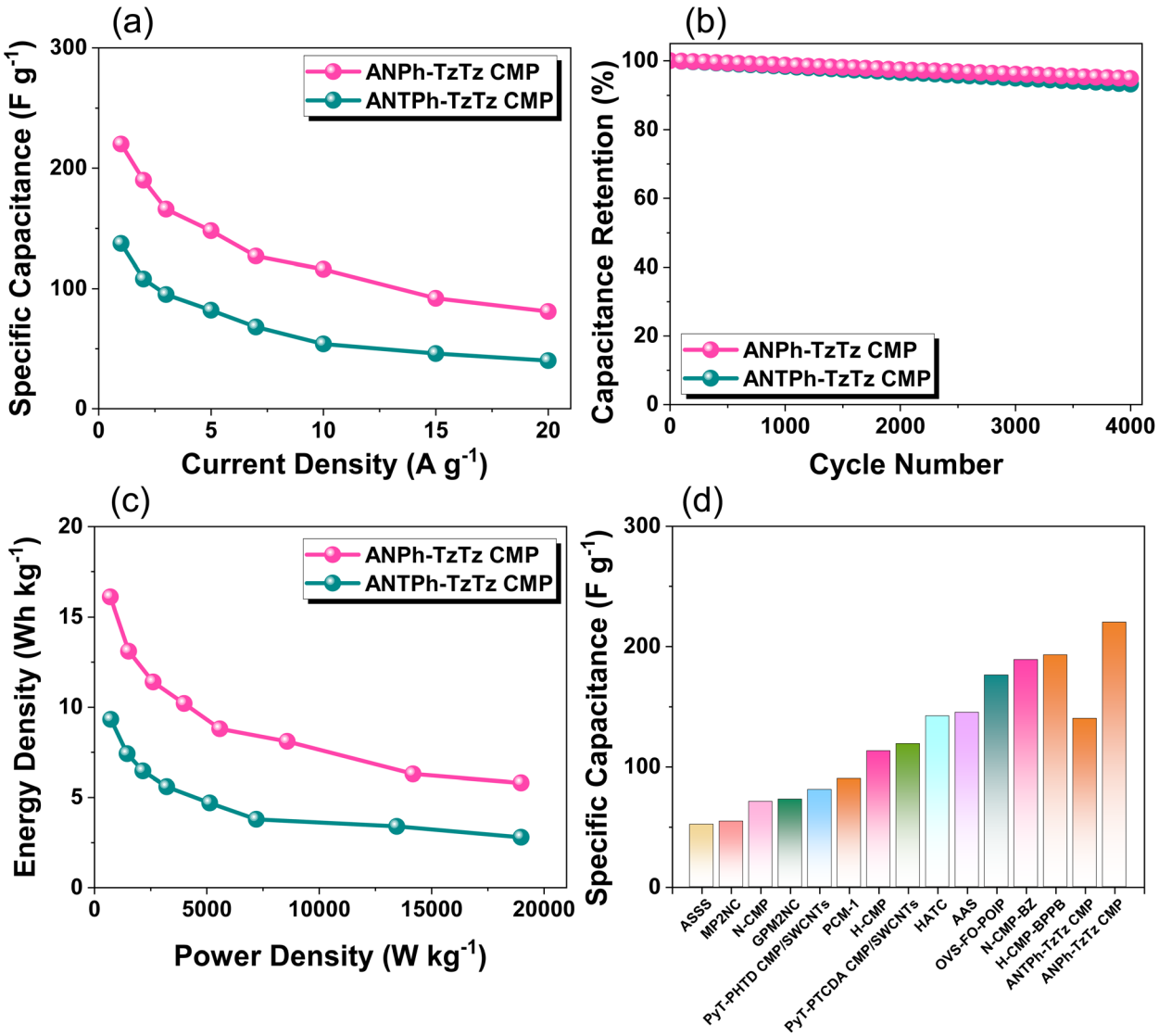

Fig. 8 (a) Specific capacitance, (b) cycling stability, and (c) Ragone plot for symmetric SC devices based on the ANPh-TzTz CMP and ANTPh-TzTz CMP. (d) Comparison of the electrochemical performance of the ANPh-TzTz CMP and ANTPh-TzTz CMP materials with previously reported systems.

values of 3.2 and 4.4 Ω for ANTPh-TzTz and ANPh-TzTz CMPs, respectively. These low resistance values highlight efficient ion transport pathways and strong electrode–electrolyte interactions, underscoring the excellent electrical conductivity and minimal internal losses within the CMP network—factors that directly support the high specific capacitance observed for both materials. The calculated results indicate that the ANPh-TzTz CMP exhibits a higher conductivity of 0.133 S m^{-1}, whereas the ANTPh-TzTz CMP shows a comparatively lower value of 0.095 S m^{-1}. Fig. S13(b) presents the equivalent circuit model for EIS fitting for CMPs.

The Bode magnitude plots [Fig. S13(c)] show a gradual decline at lower frequencies, affirming capacitive behavior, while the elevated impedance at higher frequencies corresponds to resistive limitations. Phase angle Bode plots [Fig. S13(d)] further reveal moderate knee frequencies for ANTPh-TzTz and ANPh-TzTz CMPs, which serve as a critical metric for evaluating the material's capability to sustain rapid charge–discharge cycles. These moderate knee frequencies reflect a well-balanced tradeoff between ion diffusion and surface-controlled kinetics, highlighting robust performance under high-rate operational conditions. The molecular electrostatic potential (MESP) maps offer a great deal when it comes to identifying the potential donor–acceptor regions involved in electrostatic and redox interactions. Fig. S14 displays the MESP maps of the investigated ANPh-6CHO and ANTPh-4CHO monomers that are particularly considered to design and synthesize the ANPh-6CHO and ANTPh-4CHO CMPs for supercapacitance applications. From Fig. S10, it can be inferred that zones depicted in red correspond to areas of high negative electrostatic potential, indicating sites favorable for interaction with cationic electrolyte species. These regions are typically

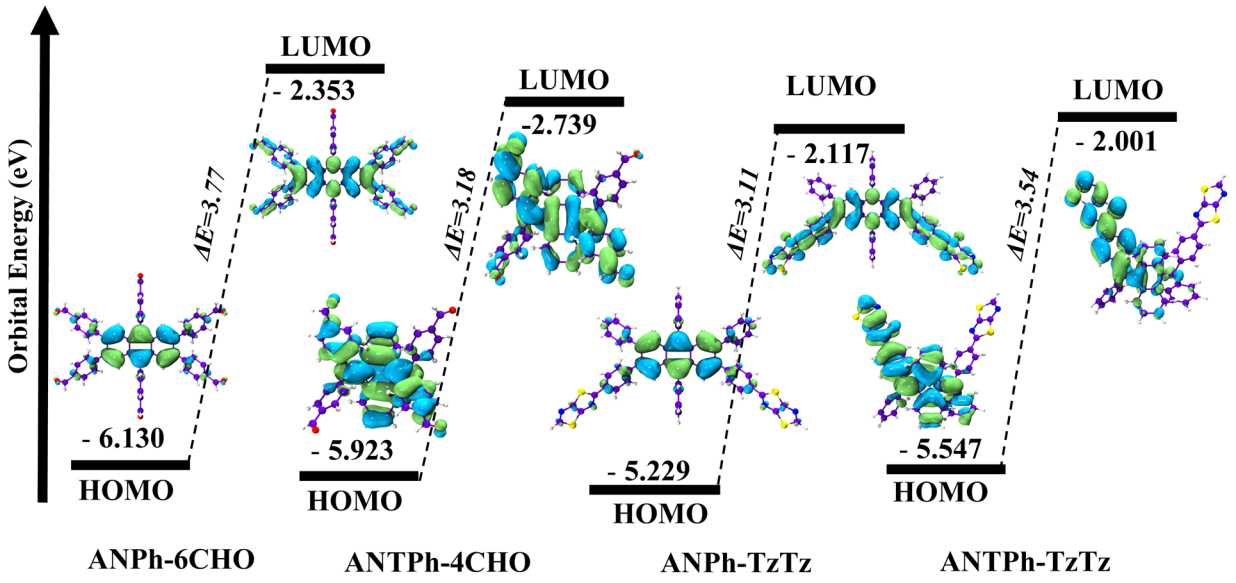

Fig. 9 The visual description of HOMO–LUMO plots of the ANPh-6CHO, ANTPh-4CHO, ANPh-TzTz CMP, and ANTPh-TzTz CMP.

associated with heteroatoms such as nitrogen and sulfur, which are known to facilitate faradaic interactions in pseudocapacitive charge storage.[77] In contrast, the blue regions represent zones of low electron density and positive electrostatic potential, which are likely to interact with anionic electrolyte species such as OH^- or BF_4^-.[78] For both ANPh-6CHO and ANTPh-4CHO, significant electron density accumulation is observed along the periphery, particularly around heteroatomic functional groups, suggesting favorable cationic binding sites. Simultaneously, the widespread blue regions surrounding the aromatic backbone cores indicate a strong potential for anionic interaction, thereby supporting dual-mode charge storage through both electric double-layer formation and redox processes.[78] This duality makes both ANPh-6CHO and ANTPh-4CHO highly promising molecular building blocks for constructing CMPs tailored for high-performance supercapacitor applications. Fig S14 illustrates the MESP maps of ANPh-TzTz CMP and ANTPh-TzTz CMPs. In the case of ANPh-TzTz, the predominant blue shading distributed around the conjugated backbone and extending toward the peripheral regions signifies areas of positive electrostatic potential, which are favorable for the adsorption of anionic species such as OH^- or BF_4^-. This uniform electrostatic environment supports efficient accommodation of anions and suggests a likely contribution from electric double-layer capacitance mechanisms. Conversely, the MESP map of the ANTPh-TzTz CMP reveals the emergence of a distinct yellow zone concentrated within the central aromatic core. This indicates a shift in the electrostatic landscape, with an increase in electron density delocalization across the core structure. Such redistribution suggests that this region may act as a favorable site for cation adsorption, potentially participating in redox-active pseudocapacitive processes.

The observed difference in charge distribution is attributed to the intrinsic structural conformation of ANTPh-TzTz CMP, which appears to alter the π-electron delocalization and modulate the electrostatic profile of the molecule. Taken together, these results suggest that the ANPh-TzTz CMP exhibits stronger anion-binding tendencies, while the ANTPh-TzTz CMP possesses structural characteristics conducive to cation interaction and charge delocalization, both of which are advantageous for the development of high-performance supercapacitor materials. Contour line (CL) mapping offers an interesting approach to visualize the distribution of electron density across the molecular framework, crucial for understanding charge transport in supercapacitance applications.[78] In contour maps, the solid lines depict the regions with the positive electrostatic potential, whereas the dashed lines correspond to the regions exhibiting negative potential. Densely packed contour lines highlight zones of high electron density, typically associated with strong π-conjugation and bonding interactions. In contrast, widely spaced contours indicate regions of low electron density, such as voids or non-bonding areas.[79] Fig. S15 illustrates the CL maps for the ANPh-TzTz and ANTPh-TzTz CMPs, respectively. As shown in Fig. S15(b), the ANPh-TzTz CMP exhibits a highly planar structure with an extended π-conjugated system [Fig. S15(a)]. This delocalization promotes efficient charge transport, as evidenced by the densely packed electron contour regions, suggesting high electrical conductivity. Such structural characteristics facilitate rapid charge–discharge cycles, making ANPh-TzTz well-suited for high-performance EDLCs. The CL map of the ANPh-TzTz CMP corresponds to the relaxed geometry of the ANPh-TzTz CMP. In contrast, Fig. S15(d) reveals that the ANTPh-TzTz CMP adopts a more twisted, non-planar geometry, likely due to steric hindrance. This deviation from planarity disrupts the uniformity of the electron density distribution, as seen in Fig. S15(c), where electron density is more localized towards one branch and the peripheral regions of the molecule. This asymmetric distribution affects the charge-transport pathways, a trend further supported by the HOMO–LUMO analysis presented in Fig. 9. The HOMO orbitals reflect the capacity of the molecular framework to donate electrons, while the LUMO orbitals

represent its tendency to primarily electrons. The energy difference between these FMOs is indicated by the conductivity and stability of the molecules (ΔE).[80] Fig. 9 illustrates the HOMO and LUMO distribution of the investigated molecular systems. Among these, the ANPh-TzTz CMP unit shows the lowest bandgap of 3.11 eV, suggesting enhanced electronic transitions and, consequently, superior electrical conductivity. These findings align well with experimental observations. Notably, the LUMO of ANPh-TzTz CMP extends uniformly from the central aromatic core toward the peripheral TzTz fragments, illustrating efficient delocalization of the electron cloud. Such a continuous π-conjugated system is highly beneficial and desired for charge transport in energy storage devices and overall conductivity.[81] In contrast, the LUMO of ANTPh-TzTz CMP appears to be predominantly localized at the periphery of the unit, particularly around the TzTz moieties, with minimal delocalization through the central core. This spatial confinement of the electron cloud limits intramolecular charge mobility. While the TzTz units act as effective electron acceptors, the overall lack of orbital continuity across the structure diminishes its charge transfer efficiency.

Conclusions

Two novel D–A CMPs, ANTPh-TzTz and ANPh-TzTz CMPs, were synthesized *via* a Schiff-base polycondensation strategy, incorporating TzTz-fused heterocyclic building blocks to enhance electrochemical performance. Electrochemical characterization, including CV and GCD measurements, revealed markedly superior capacitive behavior for ANPh-TzTz, which delivered an impressive specific capacitance of 541 F g^{-1}, significantly outperforming the ANTPh-TzTz CMP (356 F g^{-1}) at 1 A g^{-1}. When employed as electrode materials in symmetric supercapacitor configurations, the ANPh-TzTz CMP retained its advantageous performance, affording a specific capacitance of 220 F g^{-1}, whereas the ANTPh-TzTz CMP reached 137.4 F g^{-1} under identical conditions. Both CMP-based devices exhibited excellent cycling stability, retaining 95% and 93% of their initial capacitance for ANPh-TzTz CMP and ANTPh-TzTz CMP, respectively, after 4000 consecutive GCD cycles. These findings highlight the crucial role of TzTz-based electron-rich fused units in modulating the redox-active landscape and improving the charge storage properties of CMPs. This work highlights a powerful molecular design strategy for advancing high-performance organic electrode materials toward next-generation energy storage technologies.

Author contributions

Abdul Basit: investigation, writing – original draft. Mohamed Gamal Mohamed: investigation: methodology, conceptualization, supervision, writing – original draft. Hira Karim: investigation. Shiao-Wei Kuo: supervision.

Conflicts of interest

There are no conflicts to declare.

Data availability

Data will be made available on request.

Supplementary information is available. See DOI: https://doi.org/10.1039/d5ta05442g.

Acknowledgements

This study was supported financially by the National Science and Technology Council, Taiwan, under contracts NSTC 113-2223-E-110-001- and 113-2221-E-110-012-MY3. The authors thank the staff at National Sun Yat-sen University for their assistance with the TEM (ID: EM022600) experiments.

Notes and references

1 X. Wei, X. Shi, Y. Li, H. Ma, S. Ban, X. Liu, H. Liu and C. Yang, Analysis of the European energy crisis and its implications for the development of strategic energy storage in China, *J. Energy Storage*, 2024, **82**, 110522, DOI: 10.1016/j.est.2024.110522.

2 S. U. Sharma, M. H. Elsayed, I. M. A. Mekhemer, T. S. Meng, H. H. Chou, S. W. Kuo and M. G. Mohamed, Rational design of pyrene and thienyltriazine-based conjugated microporous polymers for high-performance energy storage and visible-light photocatalytic hydrogen evolution from water, *Giant*, 2024, **17**, 100217, DOI: 10.1016/j.giant.2023.100217.

3 M. Farghali, A. Osman, I. M. A. Mohamed, Z. Chen, L. Chen, I. Ihara, P. S. Yap and D. W. Rooney, Strategies to save energy in the context of the energy crisis: a review, *Environ. Chem. Lett.*, 2023, **21**, 2003–2039, DOI: 10.1007/s10311-023-01591-5.

4 M. G. Mohamed, B. Halder, P. N. Singh, A. A. K. Mohammed, P. Elumalai and S. W. Kuo, Molecular engineering and synergistic redox-active hexaazatrinaphthalene and pyrene-based conjugated microporous polymers for superior faradaic supercapacitor energy storage, *Chem. Eng. J.*, 2025, **520**, 165892, DOI: 10.1016/j.cej.2025.165892.

5 Y. Liao, H. Wang, M. Zhu and A. Thomas, Efficient Supercapacitor Energy Storage Using Conjugated Microporous Polymer Networks Synthesized from Buchwald–Hartwig Coupling, *Adv. Mater.*, 2018, **30**, 1705710, DOI: 10.1002/adma.201705710.

6 J. Duan, K. Wang, L. Teng, H. Liu, L. Xu, Q. Huang, Y. Li, M. Liu, H. Hu, X. Chen, J. Wang, W. Yan, W. Lyu and Y. Liao, Nanofibrous Covalent Organic Frameworks as the Cathode, Separator, and Anode for Batteries with High Energy Density and Ultrafast-Charging Performance, *ACS Nano*, 2024, **18**, 29189–29202, DOI: 10.1021/acsnano.4c11262.

7 M. G. Mohamed, S. U. Sharma, N. Y. Liu, T. H. Mansoure, M. M. Samy, S. V. Chaganti, Y. L. Chang, J. T. Lee and S. W. Kuo, Ultrastable Covalent Triazine Organic Framework Based on Anthracene Moiety as Platform for High-Performance Carbon Dioxide Adsorption and Supercapacitors, *Int. J. Mol. Sci.*, 2022, **23**, 3174, DOI: 10.3390/ijms23063174.

8 S. Y. Chang, A. M. Elewa, M. G. Mohamed, I. M. A. Mekhemer, M. M. Samy, K. Zhang, H. H. Chou and S. W. Kuo, Rational design and synthesis of bifunctional Dibenzo [g,p] chrysene-based conjugated microporous polymers for energy storage and visible light-driven photocatalytic hydrogen evolution, *Mater. Today Chem.*, 2023, **33**, 101680, DOI: **10.1016/j.mtchem.2023.101680**.

9 Y. Li, J. Duan, Y. Wang, L. Teng, H. Liu, J. Li, M. Liu, W. He, H. Hu, L. Wang, W. Lyu and Y. Liao, Cu-mediated bipolar-type extended π-conjugated microporous polymers for lithium-ion battery cathodes with high energy density and fast-charging capability, *Chem. Sci.*, 2025, **16**, 11311–11321, DOI: **10.1039/D4SC08244C**.

10 J. Xie, P. Yang, Y. wang, T. Qi, Y. Li and C. M. Li, Puzzles and confusions in supercapacitor and battery: Theory and solutions, *J. Power Sources*, 2018, **401**, 213–223, DOI: **10.1016/j.jpowsour.2018.08.090**.

11 M. G. Mohamed, S. V. Chaganti, S. U. Sharma, M. M. Samy, M. Ejaz, J. T. Lee, K. Zhang and S. W. Kuo, Constructing conjugated microporous polymers containing the pyrene-4,5,9,10-tetraone unit for energy storage, *ACS Appl. Energy Mater.*, 2022, **5**, 10130–10140, DOI: **10.1021/acsaem.2c01842**.

12 M. G. Mohamed, H. Y. Hu, S. Santhoshkumar, M. Madhu, T. H. Mansoure, C. W. Hsiao, Y. Ye, C. W. Huang, W. L. Tseng and S. W. Kuo, Design and Synthesis of Bifunctional Conjugated Microporous Polymers Containing Tetraphenylethene and Bisulfone Units for Energy Storage and Fluorescent Sensing of p-Nitrophenol, *Colloids Surf., A*, 2024, **680**, 132675, DOI: **10.1016/j.colsurfa.2023.132675**.

13 S. Karthikeyan, B. Narenthiran, A. Sivanantham, L. D. Bhatlu and T. Maridurai, Supercapacitor: Evolution and review, *Mater. Today: Proc.*, 2021, **46**, 3984–3988, DOI: **10.1016/j.matpr.2021.02.526**.

14 D. Lemian and F. Bode, Battery-supercapacitor energy storage systems for electrical vehicles: A review, *Energies*, 2022, **15**, 5683, DOI: **10.3390/en15155683**.

15 B. Zhao, D. Chen, X. Xiong, B. Song, R. Hu, Q. Zhang, B. H. Rainwater, G. H. Waller, D. Zhen and Y. Ding, A high-energy, long cycle-life hybrid supercapacitor based on graphene composite electrodes, *Energy Storage Mater.*, 2017, **7**, 32–39, DOI: **10.1016/j.ensm.2016.11.010**.

16 M. G. Mohamed, S. U. Sharma, P. T. Wang, M. Ibrahim, M. H. Lin, C. L. Liu, M. Ejaz, H. J. Yen and S. W. Kuo, Construction of Fully π-Conjugated, Diyne-Linked Conjugated Microporous Polymers Based on Tetraphenylethene and Dibenzo[g,p]chrysene Units for Energy Storage, *Polym. Chem.*, 2024, **15**, 2827–2839, DOI: **10.1039/D4PY00421C**.

17 C. Portet, P. L. Taberna, P. Simon, E. Flahaut and C. Laberty-Robert, High power density electrodes for carbon supercapacitor applications, *Electrochim. Acta*, 2005, **50**, 4174–4181, DOI: **10.1016/j.electacta.2005.01.038**.

18 J. Zhu, A. S. Childress, M. Karakaya, S. Dandeliya, A. Srivastava, Y. Lin, A. M. Rao and R. Podila, Defect-engineered graphene for high-energy-and high-power-density supercapacitor devices, *Adv. Mater.*, 2016, **28**, 7185–7192, DOI: **10.1002/adma.201602028**.

19 H. Yang, S. Kannappan, A. S. Pandian, J.-H. Jang, Y. S. Lee and W. Lu, Graphene supercapacitor with both high power and energy density, *Nanotechnol*, 2017, **28**, 445401, DOI: **10.1088/1361-6528/aa8948**.

20 P. G. Gautham, N. Shetty, S. Thakur, Rakshitha and K. B. Bommegowda, Supercapacitor technology and its applications: a review, *IOP Conf. Ser.:Mater. Sci. Eng.*, 2019, **561**, 012105, DOI: **10.1088/1757-899X/561/1/012105**.

21 M. Al-Sakka, H. Gualous, J. Van Mierlo and H. Culcu, Thermal modeling and heat management of supercapacitor modules for vehicle applications, *J. Power Sources*, 2009, **194**, 581–587, DOI: **10.1016/j.jpowsour.2009.06.038**.

22 M. E. Şahin, F. Blaabjerg and A. Sangwongwanich, A comprehensive review on supercapacitor applications and developments, *Energies*, 2022, **15**, 674, DOI: **10.3390/en15030674**.

23 J. Liu, C. Wu, I. D. Gates, B. Jia, Z. Huang and T. Ma, Integrated Electrode-Electrolyte Optimization to Manufacture a Real-Life Applicable Aqueous Supercapacitor with Record-Breaking Lifespan, *Energy Environ. Mater.*, 2023, **6**, 12520, DOI: **10.1002/eem2.12520**.

24 K. Dissanayake and D. K. Abeywardana, A review of supercapacitors: Materials, technology, challenges, and renewable energy applications, *J. Energy Storage*, 2024, **96**, 112563, DOI: **10.1016/j.est.2024.112563**.

25 B. Chen, L. Xu, Z. Xie and W. Y. Wong, Supercapacitor electrodes based on metal-organic compounds from the first transition metal series, *EcoMat*, 2021, **3**, 12106, DOI: **10.1002/eom2.12106**.

26 Y. He, Q. Wei, N. An, C. Meng and Z. Hu, Organic small-molecule electrodes: Emerging organic composite materials in supercapacitors for efficient energy storage, *Molecules*, 2022, **27**, 7692, DOI: **10.3390/molecules27227692**.

27 L. Wang, L. Wen, Y. Tong, S. Wang, X. Hou, X. An, S. X. Dou and J. Liang, Photo-rechargeable batteries and supercapacitors: Critical roles of carbon-based functional materials, *Carbon Energy*, 2021, **3**, 225–252, DOI: **10.1002/cey2.105**.

28 S. Samanta, S. Khatun and A. Pradhan, Morphology-dependent covalent organic polymers exhibit tunable charge storage performance in supercapacitor application, *ACS Appl. Energy Mater.*, 2023, **6**, 11890–11896, DOI: **10.1021/acsaem.3c01845**.

29 M. G. Mohamed, B. X. Su and S. W. Kuo, Robust nitrogen-doped microporous carbon via crown ether-functionalized benzoxazine-linked porous organic polymers for enhanced CO_2 adsorption and supercapacitor applications, *ACS Appl. Mater. Interfaces*, 2024, **16**, 40858–40872, DOI: **10.1021/acsami.4c05645**.

30 R. R. Salunkhe, Y. V. Kaneti, J. H. Kim and Y. Yamauchi, Nanoarchitectures for metal–organic framework-derived nanoporous carbons toward supercapacitor applications, *Acc. Chem. Res.*, 2016, **49**, 2796–2806, DOI: **10.1021/acs.accounts.6b00460**.

31 X. Liu, C. F. Liu, S. Xu, T. Cheng, S. Wang, W. Y. Lai and W. Wang, Porous organic polymers for high-performance supercapacitors, *Chem. Soc. Rev.*, 2022, **51**, 3181–3225, DOI: 10.1039/D2CS00065B.

32 P. Xu, S. Ouyang, Q. Bai, Q. Ma and Y. Zhu, A hexaazatriphenylene-based porous organic polymer for high performance supercapacitor, *J. Polym. Sci.*, 2024, **62**, 1647–1653, DOI: 10.1002/pol.20230256.

33 M. G. Mohamed, A. F. M. EL-Mahdy, M. G. Kotp and S. W. Kuo, Advances in porous organic polymers: syntheses, structures, and diverse application, *Adv. Mater.*, 2022, **3**, 707–733, DOI: 10.1039/D1MA00771H.

34 M. G. Mohamed, E. C. Atayde Jr, B. M. Matsagard, J. Na, Y. Yamauchi, K. C. W. Wu and S. W. Kuo, Construction Hierarchically Mesoporous/Microporous Materials Based on Block Copolymer and Covalent Organic Framework, *J. Taiwan Inst. Chem. Eng.*, 2020, **112**, 180–192, DOI: 10.1016/j.jtice.2020.06.013.

35 J. S. M. Lee and A. I. Cooper, Advances in Conjugated Microporous Polymers, *Chem. Rev.*, 2020, **120**, 2171–2214, DOI: 10.1021/acs.chemrev.9b00399.

36 M. G. Mohamed, I. M. A. Mekhemer, A. F. H. Selim, A. Katsamitros, D. Tasis, A. Basit, H. H. Chou and S. W. Kuo, Molecular engineering of donor–acceptor-type conjugated microporous polymers for dual effective photocatalytic production of hydrogen and hydrogen peroxide, *Mater. Horiz.*, 2025, **12**, 5917–5928, DOI: 10.1039/D5MH00735F.

37 L. Teng, J. Duan, H. Liu, X. Zhang, J. Li, Y. Li, J. Hong, W. Lyu and Y. Liao, A conjugated microporous polymer–graphene composite porous sandwich-like film for highly efficient flexible supercapacitors, *J. Mater. Chem. A*, 2024, **12**, 12423–12434, DOI: 10.1039/D4TA01603C.

38 K. G. Belekar, S. S. Patil, S. B. Bhosale, S. S. Kumbhar, G. D. Jadhav, V. G. Parale, C. D. Lokhande, H.-H. Park, P. K. Katkar and U. M. Patil, Amorphous, binder-free cobalt manganese phosphate cathodes prepared by SILAR method for asymmetric supercapacitors: Harnessing cationic synergy, *Synth. Met.*, 2025, **311**, 117800, DOI: 10.1016/j.synthmet.2024.117800.

39 W. Zhang, H. Zuo, Z. Cheng, Y. Shi, Z. Guo, N. Meng, A. Thomas and Y. Liao, Macroscale Conjugated Microporous Polymers: Controlling Versatile Functionalities Over Several Dimensions, *Adv. Mater.*, 2022, **34**, 2104952, DOI: 10.1002/adma.202104952.

40 N. Talreja, S. H. Jung and T. Y. Kim, Phenol-formaldehyde-resin-based activated carbons with controlled pore size distribution for high-performance supercapacitors, *Chem. Eng. J.*, 2020, **379**, 122332, DOI: 10.1016/j.cej.2019.122332.

41 S. V. Chaganti, S. U. Sharma, M. Ibrahim, A. Basit, P. N. Singh, S. W. Kuo and M. G. Mohamed, Redox-active a pyrene-4,5,9,10-tetraone and thienyltriazine-based conjugated microporous polymers for boosting faradaic supercapacitor energy storage, *J. Power Sources*, 2025, **627**, 235848, DOI: 10.1016/j.jpowsour.2024.235848.

42 M. M. Samy, M. G. Mohamed, S. U. Sharma, S. V. Chaganti, J. T. Lee and S. W. Kuo, An Ultrastable Tetrabenzonaphthalene-Linked conjugated microporous polymer functioning as a high-performance electrode for supercapacitors, *J. Taiwan Inst. Chem. Eng.*, 2024, **158**, 104750, DOI: 10.1016/j.jtice.2023.104750.

43 A. O. Mousa, S. U. Sharma, S. V. Chaganti, T. H. Mansoure, P. N. Singh, M. Ejaz, C. H. Chuang, J. T. Lee, S. W. Kuo and M. G. Mohamed, Designing strategically functionalized conjugated microporous polymers with pyrene and perylenetetracarboxylic dianhydride moieties with single-walled carbon nanotubes to enhance supercapacitive energy storage efficiency, *J. Power Sources*, 2025, **608**, 234624, DOI: 10.1016/j.jpowsour.2024.234624.

44 M. G. Mohamed, C. C. Chen and S. W. Kuo, Nitrogen and sulfur co-doped microporous carbon through benzo[c]-1,2,5-thiadiazole-functionalized benzoxazine-linkage porous organic polymer in CO_2 capture and energy storage, *React. Funct. Polym.*, 2025, **214**, 106286, DOI: 10.1016/j.reactfunctpolym.2025.106286.

45 M. G. Mohamed, C. C. Chen, M. Ibrahim, A. O. Mousa, M. H. Elsayed, Y. Ye and S. W. Kuo, Tetraphenylanthraquinone and Dihydroxybenzene-Tethered Conjugated Microporous Polymer for Enhanced CO_2 Uptake and Supercapacitive Energy Storage, *JACS Au*, 2024, **4**, 3593–3605, DOI: 10.1021/jacsau.4c00537.

46 M. G. Mohamed, W. C. Chang, S. W. Chaganti, S. U. Sharma, J. T. Lee and S. W. Kuo, Dispersion of ultrastable crown-ether-functionalized triphenylamine and pyrene-linked porous organic conjugated polymers with single-walled carbon nanotubes as high-performance electrodes for supercapacitors, *Polym. Chem.*, 2023, **14**, 4589–4601, DOI: 10.1039/D3PY00708A.

47 T. H. Weng, M. G. Mohamed, S. U. Sharma, S. V. Chaganti, M. M. Samy, J. T. Lee and S. W. Kuo, Ultrastable three-dimensional triptycene-and tetraphenylethene-conjugated microporous polymers for energy storage, *ACS Appl. Energy Mater.*, 2022, **5**, 14239–14249, DOI: 10.1021/acsaem.2c02809.

48 A. O. Mousa, Z. I. Lin, S. V. Chaganti, C. H. Chuang, C. K. Chen, S. W. Kuo and M. G. Mohamed, Bifunctional imidazolium linked tetraphenylethene based conjugated microporous polymers for dynamic antibacterial properties and supercapacitor electrodes, *Polym. Chem.*, 2024, **15**, 397–411, DOI: 10.1039/D3PY01303K.

49 P. N. Singh, M. G. Mohamed, S. V. Chaganti, S. U. Sharma, M. Ejaz, J. T. Lee and S. W. Kuo, Rational design of ultrastable conjugated microporous polymers based on pyrene and perylene units as high-performance organic electrode materials for supercapacitor applications, *ACS Appl. Energy Mater.*, 2023, **6**, 8277–8287, DOI: 10.1021/acsaem.3c01391.

50 M. G. Mohamed, M. Ibrahim, N. P. Chen, A. Basit, Y. C. Kao, M. O. Mousa, M. M. Samy and S. W. Kuo, Tetrabenzonaphthalene and Redox-Active Anthraquinone-Linked Conjugated Microporous Polymers as Organic Electrodes for Enhanced Energy Storage Efficiency, *ACS Appl. Energy Mater.*, 2024, **7**, 5582–5593, DOI: 10.1021/acsaem.4c01276.

51 P. N. Singh, M. G. Mohamed, M. G. Kotp, T. Mondal, S. V. Chaganti, M. Ibrahim, S. U. Sharma, Y. Ye and S. W. Kuo, Nitrogen- and Sulfur-Rich Microporous Carbons Derived from Conjugated Microporous Polymers for CO_2 Uptake, Supercapacitor Energy Storage, and Electrochemical Hydrogen Production, *ACS Appl. Polym. Mater.*, 2025, **7**, 3324–3336, DOI: **10.1021/acsapm.5c00012**.

52 M. Yoshizawa and J. K. Klosterman, Molecular architectures of multi-anthracene assemblies, *Chem. Soc. Rev.*, 2014, **43**, 1885–1898, DOI: **10.1039/C3CS60315F**.

53 J. V. Damme and F. D. Prez, Anthracene-containing polymers toward high-end applications, *Prog. Polym. Sci.*, 2018, **82**, 92–119, DOI: **10.1016/j.progpolymsci.2018.02.002**.

54 Z. Liu, A. V. Lunchev, W. Li, S. Ruan, R. Yazami, A. C. Grimsdale and H. Su, Electrochemical Properties of Anthracene-Based Lithium-Solvated Electron Solutions, *ACS Omega*, 2019, **4**, 4707–4711, DOI: **10.1021/acsomega.8b03621**.

55 D. Kong, T. Cai, H. Fan, H. Hu, X. Wang, Y. Cui, D. Wang, Y. Wang, H. Hu, M. Wu, Q. Xue, Z. Yan, X. Li, L. Zhao and W. Xing, Polycyclic Aromatic Hydrocarbons as a New Class of Promising Cathode Materials for Aluminum-Ion Batteries, *Angew. Chem., Int. Ed.*, 2022, **61**, e202114681, DOI: **10.1002/anie.202114681**.

56 M. Pavalamuthu and K. Navamani, Entropy-ruled nonequilibrium charge transport in thiazolothiazole-based molecular crystals: a quantum chemical study, *Phys. Chem. Chem. Phys.*, 2024, **26**, 16488–16504, DOI: **10.1039/D3CP05739A**.

57 F. Huang, X. Dong, Y. Wang and X. Lang, Narrowing the bandgaps of thiazolo[5,4-d]thiazole-bridged conjugated microporous polymers to capture green light for selective oxidation of amines, *Appl. Catal., B*, 2023, **330**, 122585, DOI: **10.1016/j.apcatb.2023.122585**.

58 M. Ji, C. Dong, Q. Guo, M. Du, Q. Guo, X. Sun, E. Wang and E. Zhou, Recent Advances in Organic Photovoltaic Materials Based on Thiazole-Containing Heterocycles, *Macromol. Rapid Commun.*, 2023, **44**, 2300102, DOI: **10.1002/marc.202300102**.

59 M. M. Samy, I. M. A. Mekhemer, M. G. Mohamed, M. H. Elsayed, K. H. Lin, Y. K. Chen, T. L. Wu, H. H. Chou and S. W. Kuo, Conjugated microporous polymers incorporating Thiazolo[5,4-d]thiazole moieties for Sunlight-Driven hydrogen production from water, *Chem. Eng. J.*, 2022, **446**, 137158, DOI: **10.1016/j.cej.2022.137158**.

60 S. Punyasloka, K. Higashimine and N. Matsumi, Donor–Acceptor-Based Conjugated Polymeric Active Material with Enhanced Pseudocapacitive Contribution for Ultrafast Charging of Lithium-Ion Batteries, *ACS Appl. Energy Mater.*, 2024, **7**, 5379–5389, DOI: **10.1021/acsaem.4c00404**.

61 A. O. Mousa, Z. I. Lin, C. H. Chuang, C. K. Chen, S. W. Kuo and M. G. Mohamed, Rational Design of Bifunctional Microporous Organic Polymers Containing Anthracene and Triphenylamine Units for Energy Storage and Biological Applications, *Int. J. Mol. Sci.*, 2023, **24**, 8966, DOI: **10.3390/ijms24108966**.

62 Q. H. L. Guo, N. Wang, X. Zhu, S. Jin and B. Tan, Layered Thiazolo[5,4-d] Thiazole-Linked Conjugated Microporous Polymers with Heteroatom Adoption for Efficient Photocatalysis Application, *ACS Appl. Mater. Interfaces*, 2019, **11**, 15861–15868, DOI: **10.1021/acsami.8b21765**.

63 W. Lu, L. Yan, W. Ye, J. Ning, Y. Zhong and Y. Hu, Defect engineering of electrode materials towards superior reaction kinetics for high-performance supercapacitors, *J. Mater. Chem. A*, 2022, **10**, 15267–15296, DOI: **10.1039/D2TA02930H**.

64 P. Bhojane, Recent advances and fundamentals of Pseudocapacitors: Materials, mechanism, and its understanding, *J. Energy Storage*, 2022, **45**, 103654, DOI: **10.1016/j.est.2021.103654**.

65 G. Z. Chen, Linear and non-linear pseudocapacitances with or without diffusion control, *Prog. Nat. Sci.:Mater. Int.*, 2021, **31**, 792–800, DOI: **10.1016/j.pnsc.2021.10.011**.

66 S. Halder, A. K. Pradhan, P. Sivasakthi, P. K. Samanta and C. Chakraborty, Engineering S, N-doped carbon nanosheets derived from thiazolothiazole-based conjugated polymer for efficient electrocatalytic oxygen evolution and Zn-air battery, *Mater. Today Chem.*, 2023, **32**, 101649, DOI: **10.1016/j.mtchem.2023.101649**.

67 A. Basit, M. G. Mohamed, S. U. Sharma and S. W. Kuo, Thianthrene- and Thianthrene Tetraoxide-Functionalized Conjugated Microporous Polymers for Efficient Energy Storage, *ACS Appl. Polym. Mater.*, 2024, **6**, 12247–12260, DOI: **10.1021/acsapm.4c02368**.

68 M. G. Mohamed, M. Ibrahim, N. P. Chen, A. Basit, Y. C. Kao, A. O. Mousa, M. M. Samy and S. W. Kuo, Tetrabenzonaphthalene and Redox-Active Anthraquinone-Linked Conjugated Microporous Polymers as Organic Electrodes for Enhanced Energy Storage Efficiency, *ACS Appl. Energy Mater.*, 2024, **7**, 5582–5593, DOI: **10.1021/acsaem.4c01276**.

69 G. Kwon, Y. Ko, Y. Kim, K. Kim and K. Kang, Versatile Redox-Active Organic Materials for Rechargeable Energy Storage, *Acc. Chem. Res.*, 2021, **54**, 4423–4433, DOI: **10.1021/acs.accounts.1c00590**.

70 X. Chen, H. Lv and X. Wu, Synergistic promotion of electrocatalytic activities and multilevel descriptors in nitrogen-doped graphene supported dual-atom catalysts for lithium-sulfur batteries, *Energy Storage Mater.*, 2024, **65**, 103187, DOI: **10.1016/j.ensm.2024.103187**.

71 M. Ejaz, M. G. Mohamed, Y. T. Chen, K. Zhang and S. W. Kuo, Porous carbon materials augmented with heteroatoms derived from hyperbranched biobased benzoxazine resins for enhanced CO_2 adsorption and exceptional supercapacitor performance, *J. Energy Storage*, 2024, **78**, 110166, DOI: **10.1016/j.est.2023.110166**.

72 A. Basit, Y. C. Kao, Y. A. El-Ossaily, S. W. Kuo and M. G. Mohamed, Rational engineering and synthesis of pyrene and thiazolo[5,4-d]thiazole-functionalized conjugated microporous polymers for efficient supercapacitor energy storage, *J. Mater. Chem. A*, 2024, **12**, 30508–30521, DOI: **10.1039/D4TA05908E**.

73 H. Wang, L. Liang, L. Duan, S. Sun and X. Cheng, Fabrication of MWNT@CMPs and carbonized MWNT@CMPs for supercapacitors, *Mater. Chem. Phys.*, 2019, **226**, 309–317, DOI: **10.1016/j.matchemphys.2019.01.036**.

74 M. G. Mohamed, M. G. Kotp, A. O. Mousa, Y. S. Li and S. W. Kuo, Construction of Fe- and N-Doped Microporous Carbon from Ferrocene-Based Conjugated Microporous Polymers for Supercapacitive Energy Storage, *ACS Appl. Energy Mater.*, 2025, **8**, 2389–2402, DOI: **10.1021/acsaem.4c02968**.

75 K. M. Albalawi, M. Al-Dossari, A. M. Saeedi, R. H. Althomali, G. F. B. Solre, M. Sadiq and S. U. Asif, Synergistic effects of scandium doping and N-rGO integration on titanium oxide and evaluating faradic/non faradic behavior by Dunn's model for high-performance supercapattery applications, *J. Energy Storage*, 2024, **104**, 114576, DOI: **10.1016/j.est.2024.114576**.

76 R. Anjana, P. M. Anjana, J. Alex, R. Isaac, R. S. S. Hussain and D. Sajan, Investigations on supercapacitor performance of novel ZnO-CeO_2-rGO nanohybrid prepared via hydrothermal method for energy storage applications and their charge storage mechanism, *Diamond Relat. Mater.*, 2024, **146**, 111241, DOI: **10.1016/j.diamond.2024.111241**.

77 R. Shi, L. Liu, Y. Lu, C. Wang, Y. Li, L. Li, Z. Yan and J. Chen, Nitrogen-rich covalent organic frameworks with multiple carbonyls for high-performance sodium batteries, *Nat. Commun.*, 2020, **11**, 178, DOI: **10.1038/s41467-019-13739-5**.

78 K. Amin, N. Ashraf, L. Mao, C. F. J. Faul and Z. Wei, Conjugated microporous polymers for energy storage: Recent progress and challenges, *Nano Energy*, 2021, **85**, 105958, DOI: **10.1016/j.nanoen.2021.105958**.

79 B. Kartal, A. A. Tanriverdi, U. Yildiko, A. T. Tekes and I. Çakmak, Polyimide synthesis and characterizations: DFT-assisted computational studies on structural units, *Iran. Polym. J.*, 2025, **34**, 977–999, DOI: **10.1007/s13726-024-01414-6**.

80 R. P. Morco, A. Y. Musa and J. C. Wren, The molecular structures and the relationships between the calculated molecular and observed bulk phase properties of phosphonium-based ionic liquids, *Solid State Ionics*, 2014, **285**, 74–81, DOI: **10.1016/j.ssi.2014.02.004**.

81 W. J. Fan, N. Liu, W. Q. Zhu, Y. B. Mao and M. D. Z. Tan, Design of novel conjugated microporous polymers for efficient adsorptive desulfurization of small aromatic sulfur molecules, *J. Mol. Graphics*, 2020, **101**, 107734, DOI: **10.1016/j.jmgm.2020.107734**.